Microstructural Explicit Simulation of Grain Boundary Diffusion in Depleted UO_2

by

Harn Chyi Lim

A Thesis Presented in Partial Fulfillment
of the Requirements for the Degree
Master of Science

Approved November 2011 by the
Graduate Supervisory Committee:

Pedro Peralta, Chair
Sandwip Dey
Karl Sieradzki

ARIZONA STATE UNIVERSITY

December 2011

ABSTRACT

The behavior of the fission products, as they are released from fission events during nuclear reaction, plays an important role in nuclear fuel performance. Fission product release can occur through grain boundary (GB) at low burnups; therefore, this study simulates the mass transport of fission gases in a 2-D GB network to look into the effects of GB characteristics on this phenomenon, with emphasis on conditions that can lead to percolation. A finite element model was created based on the microstructure of a depleted UO_2 sample characterized by Electron Backscattering Diffraction (EBSD). The GBs were categorized into high (D_2), low (D_1) and bulk diffusivity (D_{bulk}) based on their misorientation angles and Coincident Site Lattice (CSL) types.

The simulation was run using different diffusivity ratios (D_2/D_{bulk}) ranging from 1 to 10^8. The model was set up in three ways: constant temperature case, temperature gradient effects and window methods that mimic the environments in a Light Water Reactor (LWR). In general, the formation of percolation paths was observed at a ratio higher than 10^4 in the measured GB network, which had a 68% fraction of high diffusivity GBs. The presence of temperature gradient created an uneven concentration distribution and decreased the overall mass flux. Finally, radial temperature and fission gas concentration profiles were obtained for a fuel pellet in operation using an approximate 1-D model. The 100 μm long microstructurally explicit model was used to simulate, to the scale of a real UO_2 pellet, the mass transport at different radial positions, with boundary conditions

obtained from the profiles. Stronger percolation effects were observed at the intermediate and periphery position of the pellet. The results also showed that highest mass flux happens at the edge of a pellet at steady state to accommodate for the sharp concentration drop.

Table of Contents

Chapter Page

LIST OF FIGURES

Figure Page

Figure Page

Figure Page

Figure Page

Figure Page

I INTRODUCTION

1.1 Nuclear Energy Overview

1.1.1 History of Nuclear Power

Nuclear power tends to carry a negative image to the public. It was firstly applied as a weapon that demonstrated a devastating power in World War II. The long term radiation effect on human health, in addition to power plants accidents in Three Mile Island (1979), Chernobyl (1986) and Fukushima (2011), have all contributed to its negative image. Other than its negative public image, other power plant related issues, such as materials failure, nuclear waste storage and proliferation threat, are all challenges to the development of nuclear power.

Nuclear power was firstly applied in World War II as a weapon after Enrico Fermi from University of Chicago achieved the first self-sustaining chain reaction. It was later on applied as a mean of power generation that has the potential to replace or reduce the dependency on traditional fossil fuels. The advantages of nuclear power over fossil fuels include near zero carbon emissions and cheaper operation costs at 2.0 cents/kWh compared to 2.97 cents/kWh for coal, 5.0cents/kWh for natural gas and 12.37cents/kWh for petroleum) [2]. Over the years, nuclear energy has developed into a major power generation source in many countries including France (75%), Japan (25%) and United States (20%). It also accounts for 6% of total world energy use, the fourth largest after oil, coal and gas. Today, only eight countries are known to have nuclear weapon capability while thirty countries operate over 440 commercial nuclear power plants which show the increasing dependency on nuclear power (Fig.1.1).

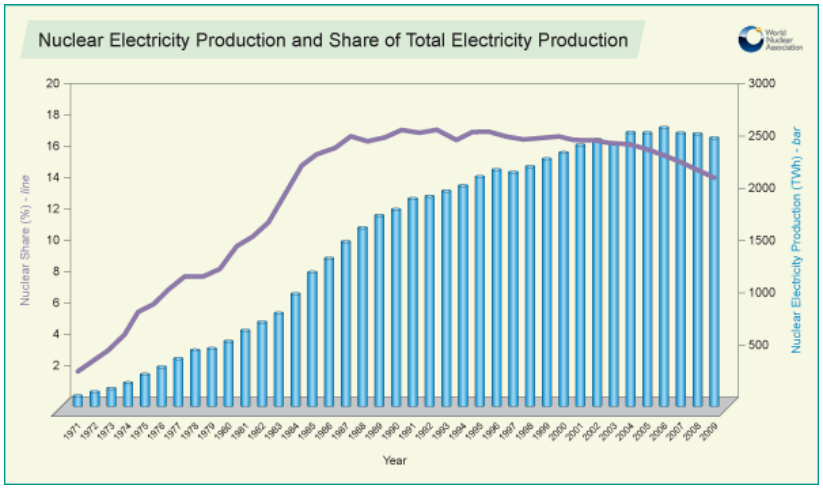

Figure 1.1: Nuclear electricity production of the world [32]

The increasing demand in energy consumption has boosted multinational collaborations to develop the next generation nuclear power plant. Today many new technologies at different scales, from completely new designs of power plants to fuel improvements for better efficiency of existing plants, are being developed to improve on nuclear power generation.

1.1.2 Issues of Nuclear Power

Some drawbacks of nuclear power include proliferation threats, nuclear wastes storage and material failure, which can limit the life time of the plants or even causes the breakdown of reactors. Each of them is briefly discussed in this section, including the strategy under development to tackle these issues.

Proliferation is a term used to describe the spread of materials that can be applied in nuclear weapons. The spent fuel of Light Water Reactor (LWR) contains Pu^{239}, which can be used to make nuclear weapons. It is desired to reduce

the production of this isotope to the minimum. A new type of fuel which burns on both UO_2 and PuO_2, termed mixed oxide fuel (MOX), was developed for the purpose. It consumes plutonium, which can be reprocessed from the spent fuel, and thus reduces the proliferation threat and the amount of nuclear waste. Other methods include mixing gamma emitter nuclides into plutonium, burning plutonium in an inert matrix fuel form to trap plutonium, or by increasing the fraction of ^{238}Pu (12%) to deter proliferation activity [33].

Waste materials from nuclear power plants remain toxic for thousands of years. To build and manage a long term storage site for the toxic wastes remains a big challenge. Most commercial nuclear reactors today store spent fuel on site, which consumes power for cooling system and is not ideal for safety purposes. Current research activities include reducing the lifetime of toxic nuclear wastes by transmutation processes and the design of a safe waste storage. To reduce the life of toxic material wastes, long lived radioactive species can be reduced through transmutation process to short lived nuclides by fission or neutron capture [34].

The extreme environment in a reactor creates a big challenge to the materials, including fuel elements, claddings as well as pressure vessels. The high temperature environment along with irradiation damages enhance creep rate, brittle failure, swelling of fuel elements, corrosion and fatigue [35]. These failure mechanisms all reduce the lifetime of the materials and need to be considered carefully during the design of a power plant.

1.1.3 Light Water Reactors (LWR)

There are many types of nuclear power plants that are designed based on different operational needs and purposes. They utilize different cooling fluids, and fuels materials. Among all reactors, the Light Water Reactor (LWR) is the most common type of nuclear power plants in the United States, and they were mostly built in 1970s. Most plants were licensed to operate for 30 to 40 years, but today, most of them are getting recertified to extend the license for another 20 to 30 years, which raises the research need for safety and better plant performance.

Light Water Reactors in the United States utilize normal water as coolant and gather the steam generated to drive turbines and were developed in the 1950s and mostly constructed in the seventies. They are one of the most common types of nuclear reactors because they are easier and cheaper to build. The only component different from a fossil fuel power plant is the nuclear reactor. Two common types of LWR are pressurized water reactors (PWR) and boiling water reactors (BWR). The difference between the PWR and BWR is the absence of a steam generator in BWR because the steam generated from fuel bundles is used directly to drive the turbine. Table 1.1 lists various LWRs developed over the years. New generations of LWRs such as the sodium fast reactor and the very high temperature reactors are designed to operate at higher temperature for better efficiency and hydrogen production capability.

Table 1.1: Genealogy of large nuclear reactors [11].

Generation I:	First nuclear electricity: EBR-I, Shippingport (US), Magnox (UK),.....1950s–1960
Generation II	Current fleet of LWRs – pressurized water (PWR) or boiling-water (BWR) (US); VVER (Russia); CANDU (a heavy-water cooled reactor) (Canada).....1970–1980
Generation II+	Current LWRs with new fuel; MOX, hydride fuel; liquid–metal bond
Generation III	LWRs of completely new design – passive safety, fewer valves, shorter piping: ABWR (GE-Toshiba), AP1000 (Westinghouse-AREVA); EPR (Europe) 1990 – present
Generation IV	Completely new designs or resuscitation of old reactor types – sodium fast reactor; (SFR); very-high-temperature reactor (VHTR)...2025 – ??

1.1.4 Nuclear Fuels

Some oxide fuels used for power generation include UO_2, PuO_2 and ThO_2. In the United States, all LWRs burn on uranium oxide, which is the earliest as well as the most common type of fuel used worldwide. A thorough understanding of its properties and behaviors under irradiation is thus very important to the operations of the current fleet of nuclear power plants.

Inside a reactor, fuel rods are composed of fuel pellets stacked inside zircaloy cladding, and the core of the nuclear reactor is composed of assemblies

of fuel rods as shown in Fig.1.2. The control rods (Ag-In-Cd) have high neutron absorption and are installed in the assembly for fission reaction management. To prevent cracks on fuel rods caused by thermal expansion and swelling of the fuel, usually a distance of 0.08 mm is kept between pellets and fuel rods. The gap is usually filled with helium gas that functions as a heat transfer medium. In operation, the fissile heavy metal atoms go through fission events and splits into fission products. Neutrons are released in the process, and they strike other atoms to sustain a chain reaction. The energy released heats up the pellet and provides thermal energy for power generation.

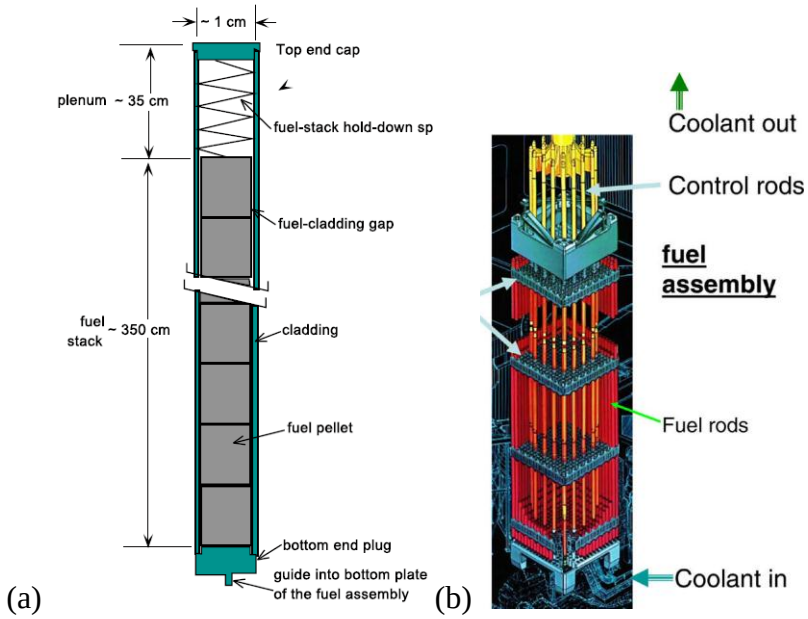

Figure 1.2: Schematic of fuel assembly for PWR. (a) cross sectional view of a fuel element. (b) Assembly of fuel rods [11]

When “burning” nuclear fuels in reactors, they go through fission processes in which the nucleus of Uranium splits into smaller fission products and release neutrons and photons that hit other nucleus to sustain a chain reaction. In nuclear power generation, a way to measure the amount of irradiation of a fuel pellet is by checking its “burnup”, which is defined as the percentage of initial heavy metal that has undergone fission. The fractional burnup (β) can be calculated as follows: $\beta = number\ of\ fissions\ /\ initial\ number\ of\ heavy\text{-}metal\ atoms\ (U\ or\ Pu)$ [22]. Burnup can also be expressed as the number of megawatt days of thermal energy released by fuel containing 1 metric ton of heavy-metal atoms (MWd/MTU). As a working rule-of-thumb, one percent burnup is approximately equal to 10^4 MWd/MTU. Typically, generation II LWRs were designed to achieve 40 GWd/MTU while some advanced designs are expected to achieve over 90 GWd/MTU [37].

1.1.5 Fuel performance

In a normal operating LWR, the edge of a cylindrical pellet is usually maintained at around 800K, limited by cladding materials, while the center of the pellet can have a temperature close to 2000 K [37]. The temperature difference between the edge of a fuel element and the coolant determines the rate of heat transfer and thus the power generated. If the coolant flow rate is not well controlled, the increase in temperature can cause damage on the zircaloy claddings or even melt the fuel rods.

Under irradiation effects and extreme conditions, the fuel properties and structures changes significantly. The changes can affect the fuel performance and sometimes cause failure. As the % burnup increases, the microstructure of fuel pellet restructures due to the high temperature and high radiation environment. Figure 1.3 illustrates the structure where a void forms at the center of the pellet due to pore migration [20], and the grains close to the center turns into a columnar shape surrounded by equiaxed grains. The grains at the edge of pellets remain the same since the temperature is lower in that region. Eventually, cracks will form as illustrated in Fig. 1.4. This change in structure makes a difference on fission gas release behaviors between low burnup and high burnup.

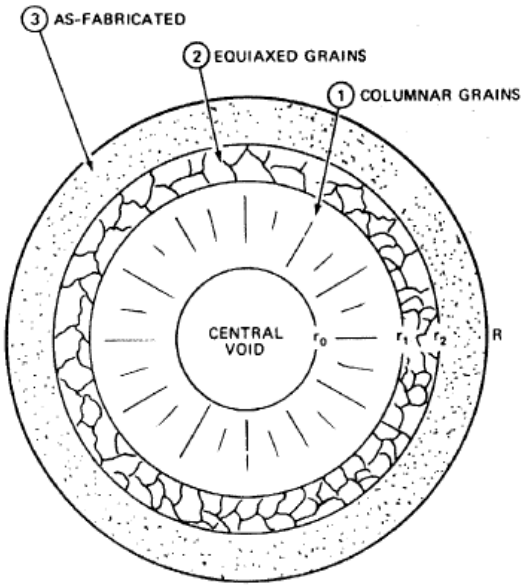

Figure 1.3: Region of a restructured fuel rod [19]

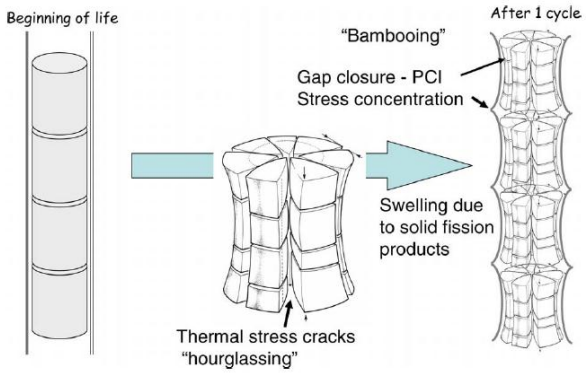

Figure 1.4: Diagram of in-pile fuel and its structure after one nuclear cycle [11]

1.1.6 Uranium dioxide properties

Uranium dioxide (UO_2), also known as uranium oxide or urania, is a black radioactive crystalline power that occurs naturally in uraninite mineral. It has a fluorite structure (CaF_2) with U^{4+} ions that form an FCC sub-lattice with O^{2-} ions occupying the tetragonal sites. One of the major advantages of UO_2 as a nuclear fuel is the stability of its fluorite structure, which gives a high melting temperature of about 2865^{o}C. The oxygen ions in UO_2 have no nuclear purpose. Table 1.2 lists some basic properties of uranium oxide.

Table 1.2: General properties of UO_2 [16]

Molecular formula	UO_2
Other names	Urania Uranium dioxide Uranous Oxide
Appearance	Black powder
Molar mass	270.03 gr/mol
Density	10.97 gr/cm^3
Melting point	2865 $^{\circ}$C (3140 K)
Solubility in water	insoluble
Crystal Structure	Fluorite
Unit cell	Cubic
Lattice parameter	0.547nm
Oxigen content	11.85 wt%

Various experimental results on UO_2 material properties were collected and organized by Mihaila's [17] and Newman's groups [18]. Material properties, including density, thermal conductivity and heat capacity, that will be helpful in the work described in this thesis are listed in Table 1.3 below. From the table, nonstoichiometric uranium oxide is expressed as UO_{2+x} with the value of x represents the fraction of excess oxygen anions. From a chemical point of view, UO_{2+x} can be treated as a solid solution of higher and lower oxidation states, such as U_3O_8 in UO_2 [55]. These excess oxygen ions tend to stay in the interstitial sites of the fluorite structure, and their presence changes the microstructure and induces cation vacancies which can affect the material properties significantly. The effects of these differences in oxygen to uranium ratio are incorporated in the measurements of UO_2 properties listed in Table 1.3. However, the value of x is taken as zero in the simulations to reduce an additional factor that can affect the formation of percolation paths, a phenomenon that will be discussed later in this chapter.

Table 1.3: A list of UO_2 properties ρ: density, C_p: heat capacity, k: thermal conductivity, Q: heat of transport of oxygen in UO_2, α: thermal expansion coefficient, E: Stiffness [17]

Property (material)	Dependence on temperature T (K) and non-stoichiometry x	Units
ρ (UO_{2+x})	$10960 \cdot (a + bT + cT^2 + dT^3)^{-3}$ $a = 0.99734, b = 9.082 \cdot 10^{-6}$ $c = -2.705 \cdot 10^{-10}, d = 4.391 \cdot 10^{-13}$ } $273\ \text{K} < T < 923\ \text{K}$ $a = 0.99672, b = 1.179 \cdot 10^{-5}$ $c = -2.429 \cdot 10^{-9}, d = 1.219 \cdot 10^{-12}$ } $T > 923\ \text{K}$	kg/m^3
C_P (UO_{2+x})	$a_0 + b_0 x + (a_1 + b_1 x)T + (1 - x)(aT^2 + bT^3 + cT^4) - (a_{-2} + b_{-2}x)T^{-2}$ $a_0 = 52.174, b_0 = 45.806$ $a_1 = 87.951 \cdot 10^{-3}, b_1 = -7.3461 \cdot 10^{-2}$ $a = -84.241 \cdot 10^{-6}, b = 31.542 \cdot 10^{-9}, c = -2.6334 \cdot 10^{-12}$ $a_{-2} = 713910, b_{-2} = 295090$	J/(mol K)
k (UO_{2+x})	$\lambda_0(T) \cdot \frac{\arctan[\theta(T,x)]}{\theta(T,x)} + 5.95 \cdot 10^{-11} T^3$ with $\lambda_0(T) = [3.24 \cdot 10^{-2} + 2.51 \cdot 10^{-4} T]^{-1}$ $\theta(T,x) = 3.67 \cdot \exp(-4.73 \cdot 10^{-4} T) \cdot \sqrt{2 \cdot x \cdot \lambda_0(T)}$	W/(m K)
Q^* (UO_{2+x})	$-1380.8 - 134435.5 \cdot \exp(-x/0.0261)$	J/mol
F (UO_{2+x})	$\frac{2+x}{2(1-3x)\cdot(1-2x)}$	
D (UO_{2+x})	$10^{-9.386 - 4.26 \cdot 10^3/T + 1.2 \cdot 10^{-3} T \cdot x - 7.5 \cdot 10^{-4} T \cdot \log(\frac{2+x}{x})}$	m^2/s
α_T (UO_{2+x})	$a + bT + cT^2 + dT^3$ $a = 9.828 \cdot 10^{-6}, b = -6.390 \cdot 10^{-10}$ $c = 1.33 \cdot 10^{-12}, d = -1.757 \cdot 10^{-17}$ } $273\ \text{K} < T < 923\ \text{K}$ $a = 1.1833 \cdot 10^{-5}, b = -5.013 \cdot 10^{-9}$ $c = 3.756 \cdot 10^{-12}, d = -6.125 \cdot 10^{-17}$ } $T > 923\ \text{K}$	m/(m K)
E (UO_{2+x})	$2.334 \cdot 10^{11}(1 - 1.095 \cdot 10^{-4} T) \cdot \exp(-1.34x)$	Pa

1.1.7 Fission gases

Fission gases and volatile fission products, such as Xe, Kr, I, Cs, are fission byproducts, and they account for a large fraction of fission yield (see Table 1.4) and thus play an important role in the operation of nuclear power plants. Many considerations need to be taken for fission gases and volatile fission products as they are generated in a large amount and change the composition, microstructures and properties of the fuels significantly. They are also the causes of some common failure mechanisms in a nuclear power plant, such as stress corrosion and fuel poisoning. Figure 1.5 shows the formation of gas bubbles in grains and how they coalesce at GBs.

Table 1.4: Fraction of elemental fission product yield in a fast neutron spectrum [19]

Chemical group	Elemental yield ^{235}U*	^{239}Pu*	15% ^{239}Pu† 85% ^{238}U
Zr + Nb	0.298	0.204	0.219
Y + rare earths‡	0.534	0.471	0.493
Ba + Sr	0.149	0.096	0.109
Mo	0.240	0.203	0.206
Ru + Tc + Rh + Pd	0.263	0.516	0.456
Cs + Rb	0.226	0.189	0.209
I + Te	0.012	0.070	
Xe + Kr	0.251	0.248	

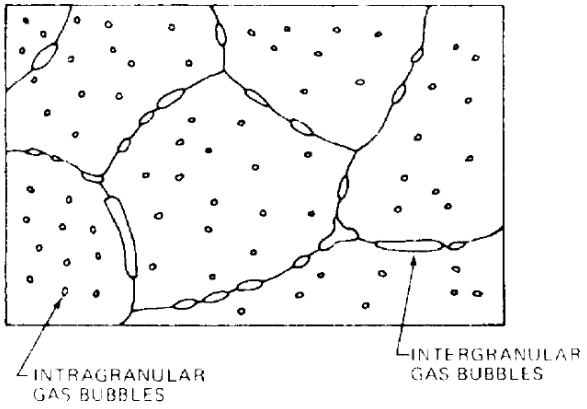

Figure 1.5: Gas bubbles forming in the grain and coalescing at GBs and triple junctions [19]

The pressure of fission gases gets larger with the increase of burnup, and there are two possible outcomes for these gases. They are either retained inside the fuel pellet or released to the gap between pellet and cladding. If the gases are released to the gap, the pressure will increase and induce stress on the cladding, which can cause stress corrosion and other failure mechanisms fatal to the reactors. They also have lower thermal conductivity than helium; therefore, they usually reduce the rate of heat transfer if released to the space between pellet and

cladding and thus decrease the efficiency of power generation. The gases released from the pellets also have higher possibility of being released to the environment and cause radiation hazards [19].

On the other hand, if the gases are kept within the fuel pellets, they tend to form bubbles within the microstructure of the pellets. The bubbles usually form in the grains and segregate to GBs and coalesce into larger bubbles. The low density gas bubbles cause the pellet to swell as the irradiation goes on. The volume of the pellets would keep growing until they touch the claddings and, again, induce stress to the claddings. If the gas bubbles link at grain boundaries, they can also cause the intergranular cracking that is seen is seen at high burnup.

Furthermore, some fission products, such as ^{135}Xe and ^{149}Sm, which have large thermal neutron absorption cross sections, are "poisonous" to fission reactions. Xenon, in particular, has a relatively large fission yield (Table 1.4) as well as a neutron absorption cross section of 2.7×10^6 barns [22] (compared to 60barns for ^{235}U). These fission products absorb neutrons from the chain reaction and thus can significantly affect the performance of the fuel. The concentration of Xe has thus become a critical factor that needs to be monitored during operation, especially during the startup and shutdown period.

As outlined in the review offered above, fission gases affect many aspects of the operation of a nuclear power plant, and it is thus very important to understand their behaviors from their production to their movement within fuel elements.

1.2 Microstructural effects on UO2 fuel pellets

Today, with the advances in characterization techniques and computing capability, research into fuel performance can be taken to the next level. In the microstructural scale, many studies have shown that the differences in free energy at different sites of a polycrystalline material, e.g., grain boundaries, can lead to anisotropy effects on their properties [21]. However, no conclusive results can be drawn yet for all polycrystalline materials and there is still a lack of experimental data for UO_2 regarding the effects of microstructure. On the other hand, most simulations are focusing on the fuel pellet-cladding interaction and the irradiation damage of surrounding materials. The goal of this study is to look into the microstructure of UO_2 and find how it can affect the transport properties of fission products.

1.2.1 Grain Boundary (GB) and Coincident Site Lattice Theory (CSL)

Grain boundaries play an important role in polycrystalline materials. The material properties at GBs are different from the lattice because of higher interfacial energy and weaker bonding. They are usually the preferred sites for corrosion, cracking as well as mass diffusion [48]. Some methods and experimental results that describe the characteristics of GBs are presented in this section.

Grain boundaries are interfaces between grains of different orientations. They are defects where the lattices in materials misalign. The difference in angles, measured between two grain orientation axes, of two adjacent grains is called the

misorientation angle. Based on the rotation axis between two grains, GBs can be categorized as tilt GBs and twist GBs. A tilt boundary has a rotation axis that is parallel to the boundary plane while the twist boundary has the axis perpendicular to the boundary plane. Grain boundaries can also be as low and high angle GBs according to the angles of misorientation. Usually when the angle exceeds 10° to 15°, it is categorized as high angle GBs. In a low angle GB, atoms are better aligned with each other while they tend to be more distorted in high angle GBs, and thus high angle GBs has higher GB energy [49].

It was discovered that certain high angle GBs with certain specific planes and misorientation angles have lattice sites that coincide between two grains, and these boundaries are expected to have a more regular structure than a general GBs. According to CSL theory, these grain boundaries can be categorized by their degree of fit (Σ) which is defined by the reciprocal of the ratio of coincidence sites to total number of sites at boundaries [48]. Figure 1.6 shows an example of the structure of a Σ5 tilt (310)/ [001] GB [12]. The effect of CSL on GB energy has been experimentally proven for many materials [21], including both metals and ceramics (Fig.1.7, 1.8). For UO_2 fuels, the effect of GBs on fission gas bubble formation has also been illustrated in Fig.1.9, where it can be seen that the bubbles developed into different shapes at different GBs of one grain.

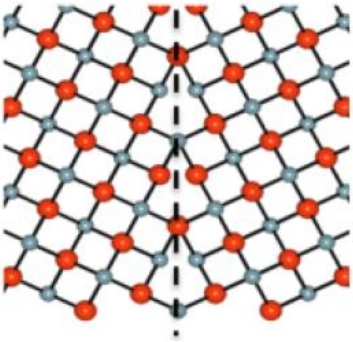

Figure 1.6: Structure of Σ5 tilt (310)/ [001] boundary [12]

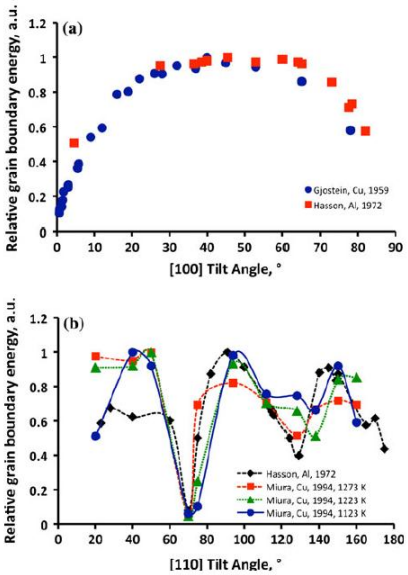

Figure 1.7: The GB energy at different misorientation angels for FCC metals (a) [100] tilt (b) [110] tilt [21]

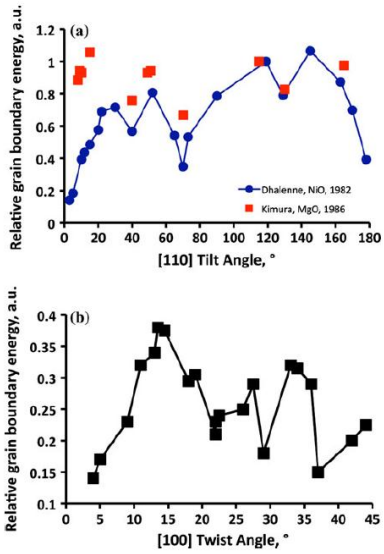

Figure 1.8: The GB energy at different misorientation angels for a ceramics (a) [100] tilt (b) [110] tilt. [21]

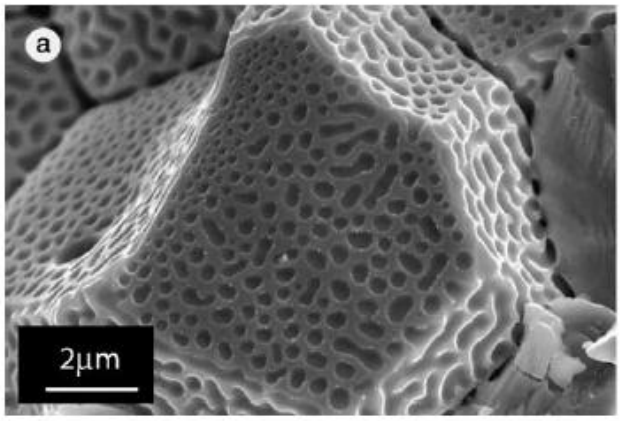

Figure 1.9: One UO_2 grain showing different shape of fission gas bubbles at different GBs [42]

1.2.2 Diffusion along Grain Boundaries

The phenomenon of GB diffusion was established as early as 1950s when Fisher [50] set up the problem by placing a thin layer of high diffusivity material

between two grains with low diffusivity (see Fig. 1.10). Constant flux was applied at the surface and by solving for a mass balance equation with Fick's law of diffusion, the GB concentration holds the form in Eq. 1.1 and bulk concentration shown as Eq. 1.2, where the C_b is concentration of GB, D_b is diffusivity of GB, D is diffusivity of the bulk, c is concentration of the bulk and δ is the GB thickness. Whipple [52] obtained the first exact solutions to this problem and it was shown that the GB diffusivity can only be obtained in terms of δD_b which shows that the thickness of GBs plays an important role in GB diffusion.

$$\frac{\partial c_b}{\partial t} = D_b \frac{\partial^2 c_b}{\partial y^2} + \frac{2D}{\delta}\frac{\partial c}{\partial x} \tag{1.1}$$

$$\frac{\partial c}{\partial t} = D_1 \nabla^2 c \tag{1.2}$$

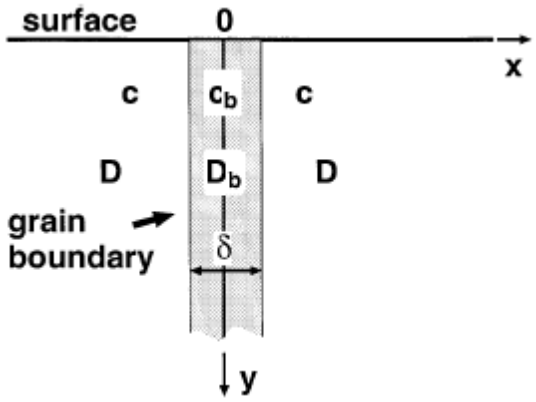

Figure 1.10: Schematic geometry in Fisher's GB diffusion model [44]

For polycrystalline materials, the GB diffusion mechanism was classified into three types by Harrison [44]. Figure 1.11 shows a schematic of the three GB diffusion types. Type A describes a case with long diffusion time, small grain size

and a high bulk diffusivity that is comparable to GB diffusivity. Under these conditions, no significant difference in concentration can be observed. Type B is the most common type of diffusion mechanism that is observed from experiments [53]. It has a deep penetration depth along GB with a simultaneous diffusion from GB to bulk. If the bulk diffusivity is negligibly small, the diffusion mechanism is a type C, which has no observable concentration gradient in the bulk.

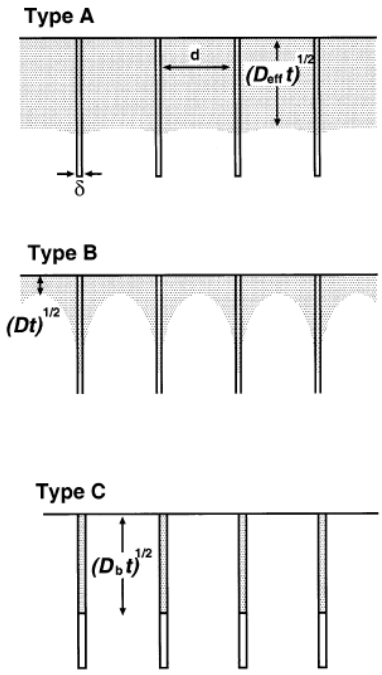

Figure 1.11: schematic illustration of type A, B and C boundary diffusion in polycrystalline materials [44]

Experimental works, as well as simulations, had been done on ceramics material with fluorite structure, such as yttria –stablized zirconia (YSZ) and cubic ZrO_2, and illustrated the effects of GBs on mass transports [54]. For nuclear fuels, uranium oxide to be specific, it was generally believed that the release of fission

gases occur mainly by the interconnections of gas bubbles at GBs. However, analysis done by Olander [20] showed that is only the case at medium and high burnup (> 20MWd/kg) when the gas atoms are trapped after migrating a distance equal or less to the size of a grain. At low burnup, GB diffusivity is the main parameter contributing to the release of fission gases with little or no effects from trapping.

1.2.3 Percolation theory of mass transport

Percolation describes the geometrical transition between disconnected and connected phases with respect to the increase of concentration of occupied sites. It deals with the number and properties of clusters, which is defined as a group of neighboring occupied sites. The percolation threshold (p_c) is the concentration at which the cluster starts to expand from one side of the system to the other. The value is dependent on the lattice geometry as well as the size of the network and can be solved mathematically. For an infinite network, the honeycomb lattice has a percolation threshold of 0.65271. The values for 3-D network are generally smaller due to the larger number of neighboring sites, and the p_c for a simple cubic network has a value of 0.2488 [56]. Percolation theory has been applied in the study of many physical properties of disordered system such as mechanical properties of gels and conductivity of metal insulator composites. Recently, it is also applied to study the diffusion mechanism in a GB network.

The effect of different diffusivity on mass transport in a GB network and the conditions that lead to percolation were studied by Chen et al. [13]. The model

was set up as an ideal, 2-D honeycomb lattice network with two diffusivity values randomly distributed to each GB. The high diffusivity (D_2) and low diffusivity (D_1) are assigned to non-CSL and CSL boundaries, respectively. The fraction of high diffusivity GBs (p) can be varied arbitrarily in this simulated network. The effective diffusivity was calculated using Effective Mean Theory (EMT) and the value was an index of macroscopic diffusivity of the GB network shown in Eq. 1.3 [13], where C_0 is a constant concentration, Q is the macroscopic mass flow rate in the vertical direction through the network, L is the width of the system and N_J is the number of boundaries.

$$D_{eff} = \frac{QL}{C_0 N_J} \tag{1.3}$$

In Fig. 1.12, the normalized concentration profile is plotted at two different diffusivity ratios with p=0.7 and the difference is obvious with the diffusivity ratio set at 10 and 10^8. The concentration distribution becomes nonlinear in Fig. 1.12b, which is the high diffusivity contrast case. The distribution of the concentration showed how the low diffusivity GBs hindered the mass flow on certain sites while increased the mass flow on others. The normalized effective diffusivity with respect to p at different D_2/D_1 ratio was plotted in Fig. 1.13. Two things can be observed here, the critical high diffusivity GB fraction p_c and the continuity of the curves for different D_2/D_1 ratio. At the fraction of about 0.65, there is an abrupt change in normalized D_{eff}, indicating the onset of percolation threshold which matches closely to the theoretical value for a honeycomb lattice. At this critical value, the curves have a sharp increase in

magnitude; moreover the increase in magnitude become discontinuous for high diffusivity contrast cases ($D_2/D_1>10^4$). These observations concluded that percolation behavior can only be observed for the high contrast GB network and the critical value of percolation threshold obtained in this simulation is at about 0.65.

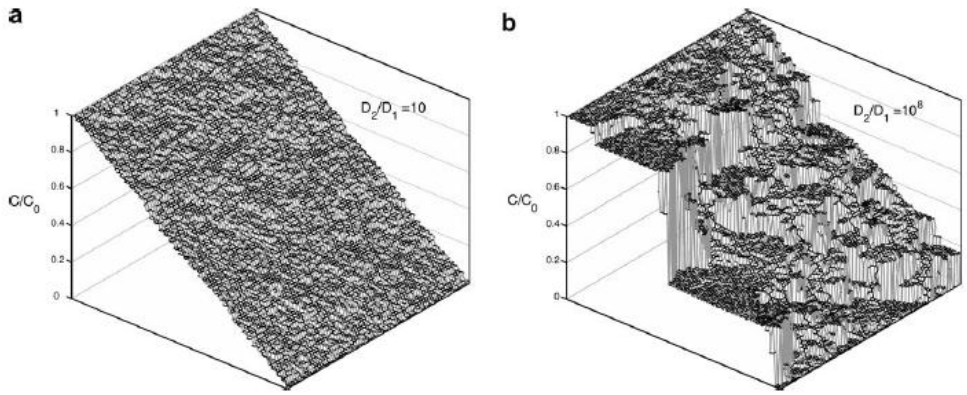

Figure 1.12: The normalized concentration profiles at two different diffusivity contrasts [13].

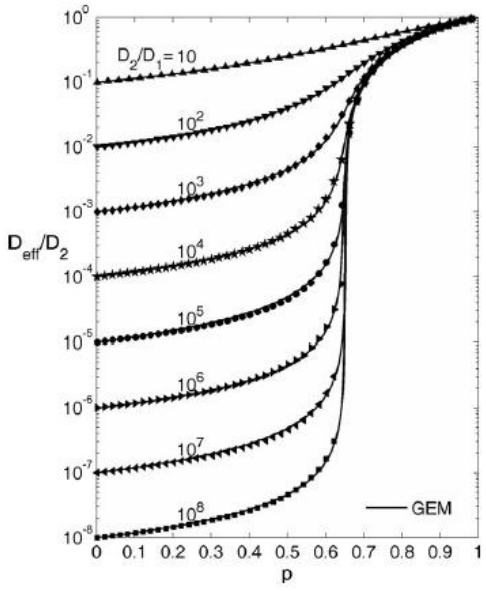

Figure 1.13: D_{eff}/D_2 over a range of high angle GB fraction [13]

Another study, conducted by Rudman et al. [6], built on the analysis described above and conducted simulations with a real microstructure of UO_2 containing 68% fraction of high diffusivity GBs. The study set up a normalized concentration profile and observed the percolation paths at different diffusivity ratios, and the results are shown in Fig.1.14, which are in fairly good agreement with Chen's. The effective diffusivity was also calculated and plotted over log (D_2/D_1), and it showed that the normalized diffusivity (D_{eff}/D_2) reached a constant value as the D_2/D_1 ratio reaches above 10^4 (Fig.1.15).

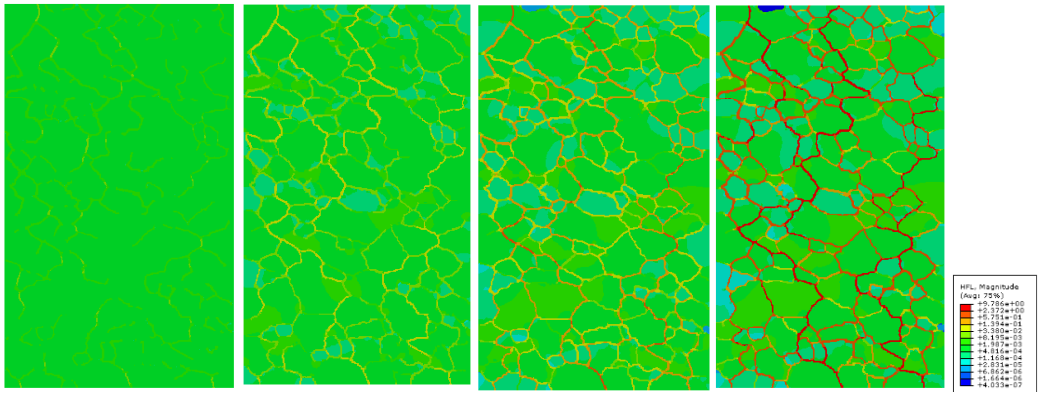

Figure 1.14: Previous 2D model showed that diffusion occurs mostly along GBs. The assigned diffusivity ratio from left to right is 10^4: 10^5: 10^6: 10^7 [6]

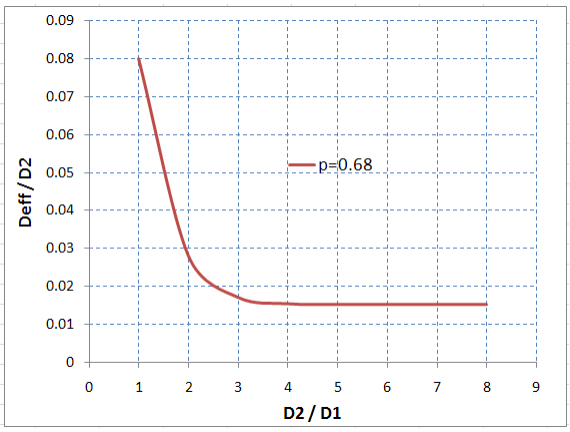

Figure 1.15: D_{eff}/D_2 vs. D_2/D_1 plots for a UO_2 sample with 68% high diffusivity GBs [6]

The model discussed here illustrated the boundary diffusion mechanisms and the formation of percolation paths. It also showed that grains contribute very little to the overall mass transport, and thus can be neglected for this simplified model. However, there exist several flaws in this model that can be improved on. First of all, as mentioned in the previous sections, the thickness of GB plays an important role in the study of GB diffusion. The model here used a 1 μm GB thickness which does not reflect the real GB thickness and can affect the calculation of concentration profiles and mass flux. The model also utilized a normalized concentration with no temperature effects, which does not reflect the real environment of a nuclear reactor. In addition, the use of "thick" boundaries is not well suited to perform calculation in 3-D. Therefore, alternatives will be sought in this work to improve in the model capabilities to overcome some of these issues.

1.2.4 The Window Method for Material Analysis

The window method in material analysis describes a technique that examines macroscopic properties of a material by simulating its behavior at the micro scale in an effort to calculate the average properties of the materials. The requirement of this type of analysis is to have a microstructure that contains enough key features that are representative of the materials being analyzed. Gao [43] illustrated the use of this technique by applying six different casting conditions to a microcell to study the effects of defects on fatigue resistance. As shown in Fig. 1.16, the microcell is embedded in the materials under different conditions, and the behavior observed in that microcell is used to estimate the overall performance of the material. A similar method will be used in this research by applying different conditions to the microstructure of UO_2 to simulate the mass transport behavior at different locations of a pellet. The details of this analysis will be discussed in the modeling procedures.

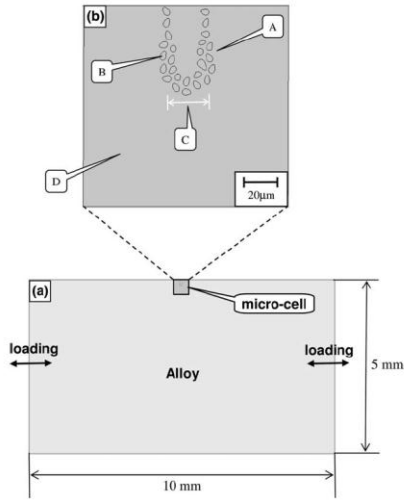

Figure 1.16: A diagram that illustrate the use of window method [43]

II OBJECTIVE

The significance and issues associated with UO_2 fuel were discussed in Chapter I. Its properties and behavior in nuclear reactors have been studied extensively over the years; however, most studies have focused on post irradiation effect and failure mechanisms in fuels with high burnup; on the other hand, very few experiments have been done to study fuel performance at its low burnup, which contains important information on fuel performance and provides the initial conditions that controls the development of the phenomena observed at high burnup. The difficulty of creating an environment comparable to that of a real reactor while still being able to remove the samples for examination after a relatively short time is a reason for limited experimental data. Therefore, simulation becomes a powerful tool for this type of study, especially with the huge advances in computing power achieved over the last couple of decades.

The objective of this research is to develop simulation tools to study the mass transport of fission products along grain boundaries of UO_2 nuclear fuel via Fickian diffusion, with emphasis on the effect of grain boundary crystallography and topology of the grain boundary network on this phenomenon for low burnup, with the effects of temperature gradient incorporated. The model will be built on a real microstructure of UO_2, with the aim of proving the feasibility of controlling fission product release in oxide fuels via grain boundary engineering.

Based on the effects of GB characteristics discussed in Chapter I, this study stresses on the importance of GB diffusion of fission products in general, and fission gases in particular, by combining characterization techniques with the

capability of conducting multi-physics simulations. The key aspects that are explored in this thesis include preliminary characterization of grain boundary structure, via characterization of distributions of misorientation angles and the CSL character, simulation of GB diffusion to observe the effect of temperature gradient on GB diffusion and percolation behavior, and lastly, simulating the behaviors of mass transport at different radial position of a pellet by the window method.

The created model is, to the best of the author's knowledge, the first finite element model of mass transport over a grain boundary network that is built on a real microstructure of UO_2 with experimentally obtained material properties incorporated. The addition of heat transfer gives the ability to simulate the high temperature gradient environment in a fuel pellet, and it also makes all the temperature dependent properties more representative. In the future, more complex geometry and physics can be built on this model to have an even more sophisticated study of mass transport in UO_2 fuels.

III EXPERIMENTAL AND MODELING PROCEDURES

To achieve the objective of examining mass transport through the grain boundaries (GB) at low burnup level, this study combines characterization techniques with the capability to do multi-physics simulation. The first step was the use of serial sectioning techniques and visualization software to reconstruct the microstructure of the d-UO_2 sample. The work described here is divided into two parts: experimental procedures and modeling procedures. In the experimental procedures, the preparation techniques of the UO_2 sample studied as provided, as well as the characterization techniques used and the type of information retrieved from them. In the modeling procedures, the model reconstruction using real grain structure obtained from EBSD is described as well as the procedures to set different parameters and boundary conditions in the models. The reconstructed model is used to conduct finite element analysis and to simulate the mass transport phenomenon in the reconstructed grain boundary network.

3.1 Experimental Procedures

This part of the work focuses on data collection starting from UO_2 fabrication procedures to the sample preparation work for microscopy. Scanning Electron Microscopy (SEM) and Electron Backscattering Diffraction (EBSD) are used heavily in the characterization work, and the both techniques combined reveal grain structure and information of misorientation angles at GBs from the area of interest.

3.1.1 Sample Preparation

Depleted UO_2 pellets 3mm in diameter were fabricated and supplied by Los Alamos National Laboratory (LANL). The fabrication process started with feedstock powder milled and sieved by Sigma Aldrich Group. Each of the 3mm diameter UO_2 pellet was produced using approximately 0.95 g of the power, pressed in a 6mm die set at 240MPa and dwelled for 60 seconds. The pellets were sintered under a constant flow of ultra-high purity (UHP) Argon in a dilatometer with a heating ramp of 20°C/min, with no holding time at a maximum temperature of 1680°C.

To prepare the pellet for SEM imaging, one pellet was mounted in epoxy and sectioned in its transversal direction. The mounted sample was then ground with 320 to 1200 grit SiC paper, subsequently, using water as lubricant. The sample was then polished 5 minutes with 3 µm diamond pastes, 3 minutes with 1 µm diamond paste and then 3 minutes with 0.25 µm diamond pastes, all with polypropylene as lubricant. Finally, the sample was polished for 20 minutes with 0.04 µm colloidal silica. The polished sample was rinsed in water and then ultrasonically cleaned with isopropanol, and it is now ready for characterization.

3.1.2 Microstructure Characterization

Scanning Electron Microscopy was used to examine the microstructure of the sample and to select the area from which to collect EBSD data. It was discovered that an electron beam set at 20keV with an exposure time of 0.015 seconds gave the best image quality [31], and thus the conditions were used

throughout the data collection process. In the EBSD technique, the backscattered electrons, which contain diffraction information, were detected. The data were collected with 0.75μm step size with 95% confidence of getting correct indexes, as estimated by EDAX-TSL OIM^{TM} analysis software. During data analysis, minimum grain size of the scan was set as 10 pixels in order to avoid "artificial" grains at poorly indexed points next to small pores and cracks. The diffraction patterns were shown as Kikuchi bands of which the angles and the band width represent the crystalline structure. Finally, the grain structures were shown in an Inverse Pole Figure (IPF) map with the colors of grains representing their orientations. Figure 3.1 is a schematic of how EBSD data are collected, and an example of a grain structure obtained from EBSD is shown in Fig. 3.2.

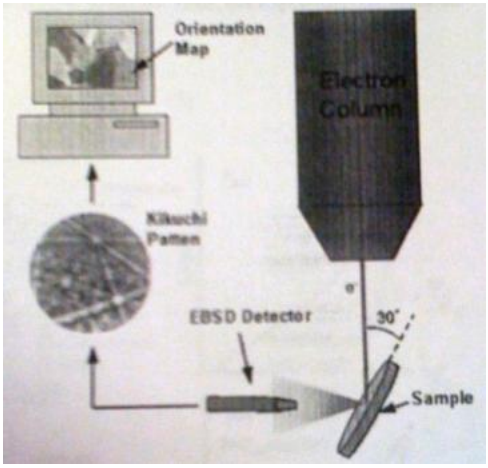

Figure 3.1: An illustration of the OIM technique

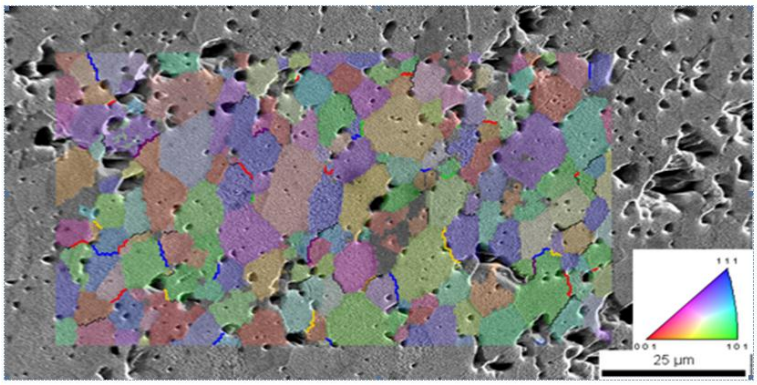

Figure 3.2: SEM and EBSD images of a depleted uranium oxide sample with 86% theoretical density. The grain orientations are represented by its colors and the CSL GBs are highlighted in red (Σ3), yellow (Σ5), green (Σ7), blue (Σ9), purple (Σ11) and black (other special GBs) [31].

An initial scan over an area 400 µm x 400 µm was made to determine the minimum area needed for serial sectioning. The area needed to be statistically representative of the sample and contains enough information on porosity, triple junctions and grains. Representative element analysis was conducted on the initial scan [30, 31] and an area of 200µm by 400µm was chosen for statistical analysis, which included grain size distribution, grain boundary distribution and misorientation angles distributions. An area of 60 µm x100 µm was down selected for serial sectioning after the analysis. For studying the mass transport along GBs, features, such as regions with clusters of small grains and large pores, were avoided in the selection process. The area was also chosen to have the average grain size and CSL fraction comparable to the overall sample in order to represent the general microstructure. The selected area is shown in Fig. 3.3.

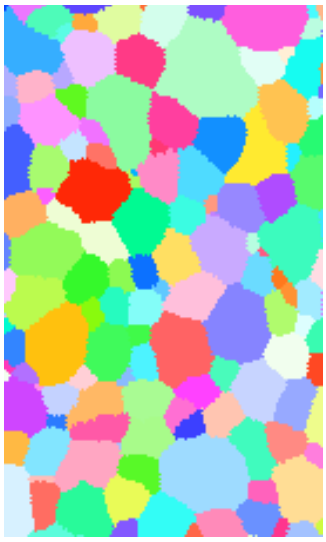

Figure 3.3: The 60 µm x 100 µm area selected for GB network reconstruction [31]

3.2 Modeling Procedures

The modeling procedures began with the reconstruction of serial sectioning slices and it went through the steps of setting up the model for finite element analysis, which included how the material properties were set up and assigned to materials and GBs, the calculation of heat and mass generation of a pellet in a power plant and lastly, the way in which boundary conditions were set up for different simulations.

3.2.1 Reconstruction of Grain Boundary Surface

Reconstructing the microstructure of UO_2 pellet is an essential step for creating a model for finite element analysis. Previous simulation (see Fig. 1.14) was created on a 2-D microstructure image with GB thickness of 1µm in order to visualize the flux along GBs. However, the real thickness of GB has a size

comparable to lattice parameter of the material which is orders of magnitude smaller than 1μm. This difference can affect the overall diffusion behavior significantly. Moreover, it is also difficult to interpolate the thickness in a 3-D model reconstruction. To avoid these issues, a method to create a GB network with surface elements that have no "physical" thickness in the mesh was developed. The EBSD images (Fig. 3.3) were replicated and stacked on together, and the stacked images were imported into AVIZO™ software, where each grain was labeled and assigned with a material ID (Fig. 3.4). AVIZO™ software has the ability to interpolate the geometry in between stacked images, and with two identical images, the interpolated grains go straight down through the thickness and created this 2+1/2 dimensional geometry, which allows the 2-D simulation while keeping the GBs as surface elements. The surface elements allowed COMSOL™ to assign properties to edges and boundary planes as a 3-D geometry while preserving the properties of a 2-D network. It was desired to keep this study a 2-D problem to observe the diffusion behaviors in 2-D spaces before conducting a 3-D simulation since there was not enough data to obtain a reliable 3-D network.

(a) 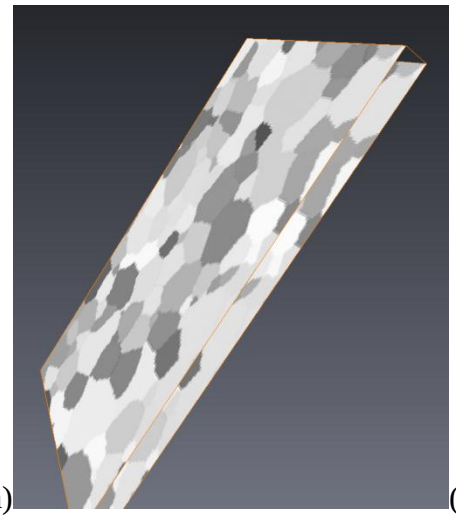 (b) 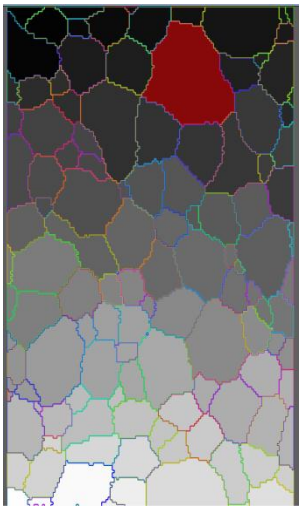

Figure 3.4: (a) Stacking two identical EBSD maps (b) Labeling grains in AVIZO^{TM}. Each grain is assigned to a material shown in different colors

In Chapter I, the 2-D, single physics study of UO_2 microstructure [6] has shown the dominance of GB diffusion when compared to grains as shown in Fig.1.14, so to emphasize on the effects of GB misorientation, CSL distribution and percolation theory on mass transport in GB network, this study keeps only GB elements in the simulation. The 3-D reconstruction created with AVIZO^{TM} was exported to Hypermesh software (Fig. 3.5a) and the GB network was extracted from the exported geometry by removing grain elements. The mesh elements were generated by AVIZO^{TM} in the reconstruction process (Fig. 3.5b), and the meshed GB structure was transformed into the NASTRAN format, which is a meshed geometry ready for COMSOL^{TM} simulation.

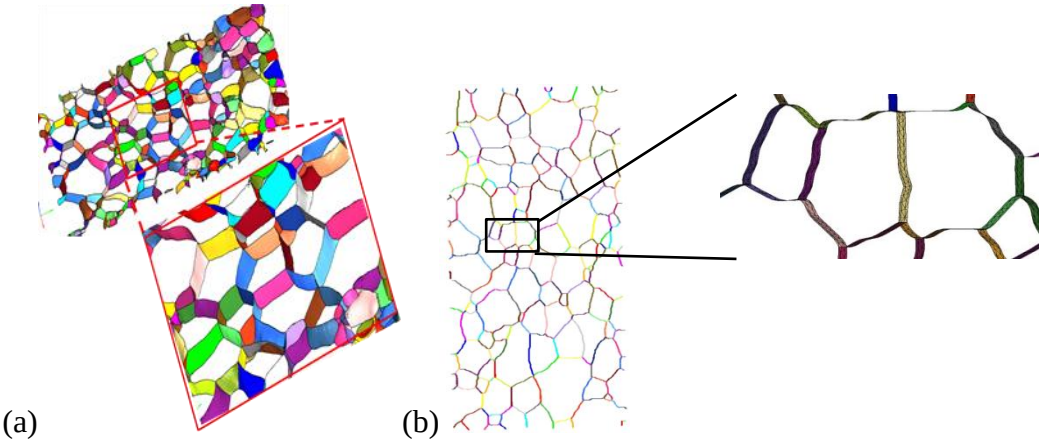

Figure 3.5: (a) The microstructure of GB network obtained from Hypermesh (b) The GB mesh elements are generated in the reconstruction process

3.2.2 UO_2 Material Properties and GB properties.

Various UO_2 material properties were collected and organized by Mihaila's [17] and Newman's groups [18]. Material properties, including density, thermal conductivity and heat capacity, that were applied in the simulation are listed below. All values here are calculated for stoichiometric UO_2; hence the x value for UO_{2+x} is assumed to be zero for our sample.

Density:

$$\rho_{UO_2}\left(\frac{kg}{m^3}\right) = 10960 \times (a + bT + cT^3 + dT^3)^{-3}$$

For T < 923K, a = 0.997, b = $9.802*10^{-6}$, c = $-2.705*10^{-10}$, d = $4.391*10^{-13}$

For T > 923K, a = 0.997, b = $1.179*10^{-5}$, c = $-2.429*10^{-9}$, d = $1.219*10^{-12}$

Thermal Conductivity:

$$k_0(\frac{W}{mK}) = (3.24*10^{-2} + 2.51*10^{-4}T)^{-1} + 5.95\times10^{-11}T^3$$

Heat Capacity:

$$C_p^{UO_2}(\frac{J}{kgK}) = 264.256 + 0.047T$$

Diffusivities were assigned to GBs based on misorientation angles, CSL types and the percolation theory described by Chen [13]. According to this work, the ratio between high diffusivity (D_2) and low diffusivity (D_{bulk}) along with the fraction of high diffusivity GBs (*p*) within the network determine whether or not the network has percolation behaviors. The value for *p* can be calculated from the characterization results, and the D_2/D_{bulk} ratios were assigned directly as inputs to the simulation.

For this model, various GBs in the microstructure were categorized into 3 different groups – High diffusivity (D_2), Low diffusivity (D_1), and Bulk diffusivity (D_{bulk}) GBs. In Fig. 3.6, experimental work showed that the diffusivity increases with the increase of misorientation angle and peaks at about 45° due to the symmetry of the cubic system. Diffusivity at GBs is associated with its free energy, and the increase in diffusivity agrees with the experimental results that showed the increase of GB energy with misorientation angle for both metal and ceramics [21]. The data from Fig. 3.6 was then divided into three regions and assigned to D_{bulk}, D_1 and D_2 based on the misorientation angles.

The misorientation angle for each GB was identified from characterization results, and the diffusivities were assigned accordingly. The CSL GBs are

grouped into the bulk diffusivity regime with Σ values ranging from 3 to 11 as they are the most dominant ones in terms of number fractions. The higher sigma values are not considered in this model because they only account for a small proportion and the differences in GB energy are not as significant as low Σ GBs.

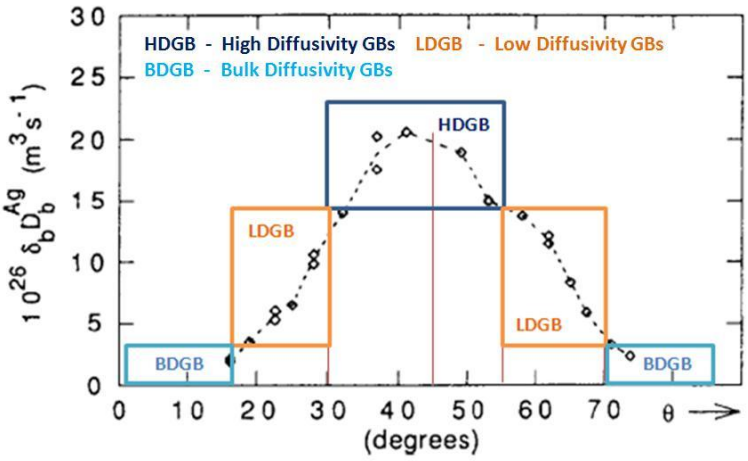

Figure 3.6: Grouping the GB Diffusivity based on their diffusivity coefficients [23].

3.2.3 Temperature profile

The effect of temperature plays an important role in the diffusion process. Inside a pellet for LWR, the local temperature gradient can be as high as 10^4 °C/cm [19], which implies that the material properties, especially diffusivity, can be very different depending on the location of a pellet. In order to observe fission gas diffusion from the center of a pellet to its edge, the temperature profile across the radius needs to be quantified.

First of all, the temperature profile of the pellet can be derived from Fourier's Law of thermal conduction (Eq. 3.1) and its partial differential equation for cylindrical shape holds the form shown in Eq. 3.2.

$$q'' = \left(\frac{w}{cm^2}\right) = -k\nabla T \tag{3.1}$$

$$\frac{1}{r}\frac{d}{dr}\left(rk\frac{dT}{dr}\right) + q''' = 0 \tag{3.2}$$

Where k is thermal conductivity, r is the distance from the center of cylindrical pellets and q''' is the volumetric heat generation. Note that, in principle, the values of k and q''' are both temperature dependent and thus also functions of r. In order to understand the rate of fission gas migration, they can be taken as constants for simplicity of the calculations while still obtaining a good estimate of the results [1]. The value of k is taken as an average between the highest and the lowest temperature of a typical LWR [19] and the value was calculated to be 0.033W/cmK. The detail of calculating the value for q''' will be discussed in the next section. Equation 3.2 was then solved by applying boundary conditions: $T(r = R_0) = T_s$ and $\frac{d}{dr}T(r = 0) = 0$, where R_0 is the radius of the pellet. The temperature profile is obtained in Eq. 3.3.

$$T - T_s = \frac{1}{4}\frac{q''' R_0^2}{k}\left(1 - \frac{r^2}{R^2}\right) \tag{3.3}$$

3.2.4 Heat generation rate for the pellet

Heat generation rate controls the temperature profile. The volumetric heat generation is a function of fission reaction rate density multiplied by the

recoverable energy released per fission event [19], and the equation applicable to a bare uniform cylindrical pellet is shown in Eq. 3.4 [22].

$$q'''(r) = w_f \sum_f \Phi_0 J_0\left(\frac{2.405 r_f}{R}\right)\cos\left(\frac{\pi z}{H}\right) \quad (3.4)$$

Volumetric heat generation q’’’(**r**) is measured in W/cm^3, w_f is the recoverable energy released per fission event, Σf is the macroscopic nuclear fission cross section, Φ_0 is the neutron flux, J_0 is a Bessel Function of the First Kind, r_f is the pellet radius, and finally, *R* and *H* are the effective core dimensions. Figure 3.7shows the flux profile over the radius as well as the axis of the pellet. Note that the reflected region is due to the fluctuation due to coolant bypass flow, additional moderators or a blanket of fertile material from reactor design, and the effects are not considered in this study.

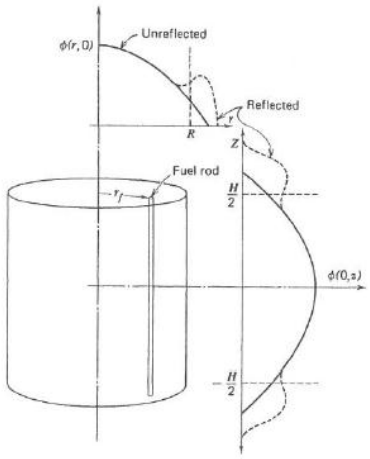

Figure 3.7: flux contribution in a cylindrical core [22]

This study takes the highest flux value, which is located at the center and the middle of the pellet, for safety purposes. To simplify the calculation, the linear power density q’ can be defined in terms of q’’’ [19].

$$q' \equiv \pi r_f^2 q'''$$ (3.5)

Reactors fueled with UO_2 have a limited q' value of 660W/cm [22], and most of the present power reactors are usually designed to operate at 460-500W/cm under normal operating conditions [22]. If we use the higher bound of the design value, i.e., 500W/cm, and with the pellet radius of 1.5mm, the volumetric heat generation is calculated to be close to 7000 W/cm^3. The temperature profile as a function of radius was then obtained and plotted. Mass transport is affected significantly by temperature, and the large temperature difference would generate different results at different radial positions. It is thus desired to model the behaviors at different locations of a pellet with Window Method. The obtained temperature profile will help determine the temperature boundary conditions needed to set up the simulation.

3.2.5 Concentration Profile

Similarly to the temperature profile, the concentration profile can also be derived from Fick's first law for mass flux which holds a similar form to Fourier's Law: $j = -D\frac{dC}{dx}$ where j is mass flux, c, is concentration and D is the diffusivity of fission gas, which cannot be taken as a constant, since it has Arrhenius temperature dependence. The partial differential equation for cylindrical geometry has the following form where H is the volumetric fission gas generation rate:

$$\frac{1}{r}\frac{d}{dr}(rD\frac{dC}{dr}) + H$$ (3.6)

Equation 3.6 can be simplified by taking an integral over r. The slope of concentration profile at the center of pellet is zero. Taking the integral over r once and applying this boundary condition, Eq.3.6 can be simplified as Eq. 3.7.

$$\frac{d}{dr}C = \frac{-Hr}{2D} \tag{3.7}$$

Integrating this equation analytically becomes more complicated than solving the temperature profile because the diffusivity D is a function of temperature and thus a function of radius. It can be expressed as $D = D_0 \exp\left(\frac{-Q}{RT}\right)$, where D_0 is a diffusivity constant, Q is the activation enthalpy and R is a gas constant. Note that T is function of position given by expression obtained in the previous section. Substituting temperature profile obtained from Eq.3.3 into the diffusivity term with, we get:

$$\frac{dC}{dr} = \frac{-Hr}{2D_0} \exp\left[\frac{Q}{R*\left(T_s + \frac{1}{4}\frac{q'''R_0^2}{k}(1-\frac{r^2}{R_0^2})\right)}\right] \tag{3.8}$$

Experimental results of fission gas diffusivity in UO_2 fuels were obtained by Turnbull [26] as well as D. Davies and G. Long [27]. Both experiments have an agreement on the overall intrinsic diffusivity as expressed in Eq. 3.9. The irradiation induced diffusivity term is assumed to be negligible at low burnup levels. There is also a thermal diffusion term in the overall diffusivity that is not considered in the scope of this study.

$$D = 7.6\times10^{-6}\exp(\frac{-70000}{RT})(cm/s^2) \tag{3.9}$$

The volumetric rate of fission gas generation can be obtained from the fission rate density $\dot{F}(\frac{\text{fission}}{\text{cm}^3\text{s}})$. At a power generation of 7000 W/cm^3, as calculated in the previous section, $\dot{F}$ was calculated to be $2.18\text{x}10^{14}(\frac{\text{fission}}{\text{cm}^3\text{s}})$, assuming each fission event produces 200 MeV of energy [19]. According to Meek and Rider [28], the total fraction, Y, of stable fission products accounts for 25% for both Uranium and Plutonium fission events. The unstable fission products, which have very short half-life, are ignored in this study, and the value of H is then 0.25 multiplied by $\dot{F}$, which gives the value of $5.46\text{x}10^{13}(\frac{\text{atoms}}{\text{cm}^3\text{s}})$ or $9.07\text{x}10^{-11}(\frac{\text{mole}}{\text{cm}^3\text{s}})$. The values are substituted into Eq. 3.8, and the concentration profile was solved numerically and plotted using Mathematica.

To work with surface elements, the obtained concentration values were converted into surface concentration before it can be applied to the model. The concentrations were multiplied by the thickness of GB which is assumed to be two lattice parameters in length (~1nm).

3.2.6 Boundary Conditions and the Window Method

In the simulations, boundary conditions are set up in several different cases to simulate different scenarios. All simulations were performed setting boundary conditions at top and bottom of the geometry and keeping the sides insulated to make it a macroscopic 1-D problem (Fig. 3.8). The values of

temperature and concentration, calculated in the previous sections, simulate the real environment inside a reactor.

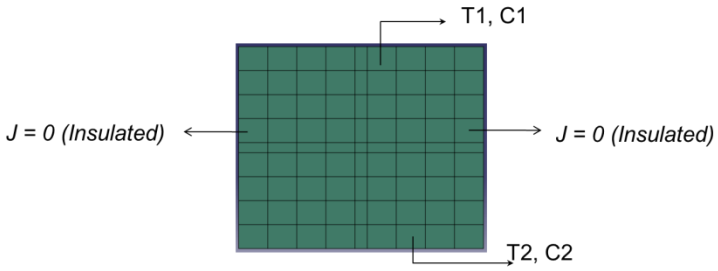

Figure 3.8: Schematic of boundary conditions set up. T: temperature, C: concentration, J: mass flux

The window method was applied to the simulations. It was set up by placing the created geometry at different radial positions inside the pellet to simulate the behavior under different environments. The boundary conditions were set up by applying the values obtained from the macroscopic temperature and concentration profiles. It should be noted that the geometry of the reconstructed GB network is rectangular, while the real pellet is a 3mm diameter cylindrical rod. The temperature and concentration gradients are linear in the rectangular geometry but not in a cylinder as its surface area increases with radius. In order to better represent the real case scenario, the 100micron by 60 micron reconstructed area is used to linear fit different locations of a pellet along its radius.

The 0.15cm pellet radius is divided into 15 sections, each one represented by the 0.01cm long rectangle. Temperature and concentration boundary conditions are set up according to the radial positions where the geometry is

placed, and the fission gas behaviors at different locations of pellets can thus be simulated. Figure 3.10(a) demonstrates how the temperature profile from 0 to 0.01cm is fitted with a straight line, and the 15 line fits are plotted in Fig. 3.9(b), which shows that 15 linear regions provide a good approximation to the original curve. The same approach is done for the concentration profile. The values for all boundaries conditions were obtained from the temperature and concentration profiles derived.

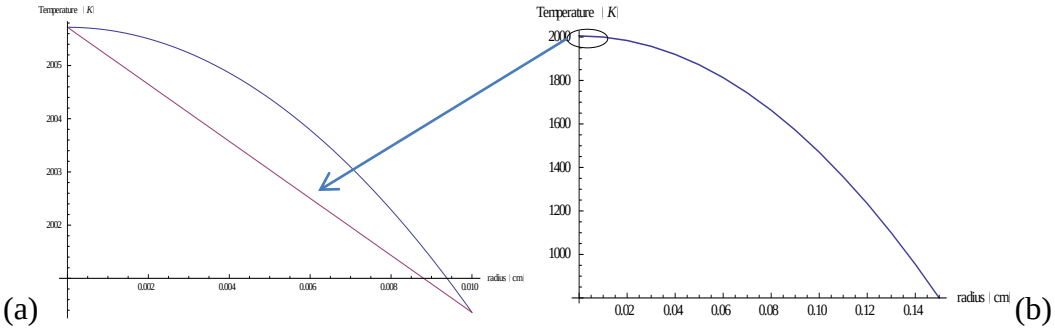

Figure 3.9: (a) Line fit of temperature profile from r=0 to r=0.01cm. (b) The line fits along the whole radius.

IV RESULTS AND DISCUSSION

This chapter presents the results of the characterization of UO_2 sample and the simulation results obtained with different conditions described in the previous

chapter. The preliminary characterization provided information about the grain structure and distribution of different GBs. In the simulation part, to address the different physical phenomena that affect the mass transport of fission products along GB networks, models are set up in three different ways: constant temperature, effects of temperature gradient, and a combination of both of them with the window method to simulate mass transport at different radial positions of a fuel pellet. Each model setup is assigned with the same material properties but different boundary conditions based on the scenarios and all models are simulated with different diffusivity contrasts to study the potential onset of percolation on the GB network.

4.1 Preliminary Characterization

This section provides some background information about the microstructure of the sample in terms of the porosity, grain sizes and GB distribution from SEM and EBSD characterization. The results of microstructure reconstruction along with data on the different types of GBs and their distribution are also presented here.

4.1.1 Scanning Electron Microscope and EBSD analysis

The SEM and EBSD images of the 400μm by 400μm scan used to extract microstructure for this work are shown in Fig. 4.1. Regions with clusters of small

grains and pores as well as large pores were observed. The small grains could have been generated during the sintering stages [41]. The small grains and pores were not distributed uniformly through the microstructure and thus are not representative of the overall microstructure of the sample. A representative element analysis was conducted by Rudman [31], and an area of 200μm x 400μm was selected for statistical analysis.

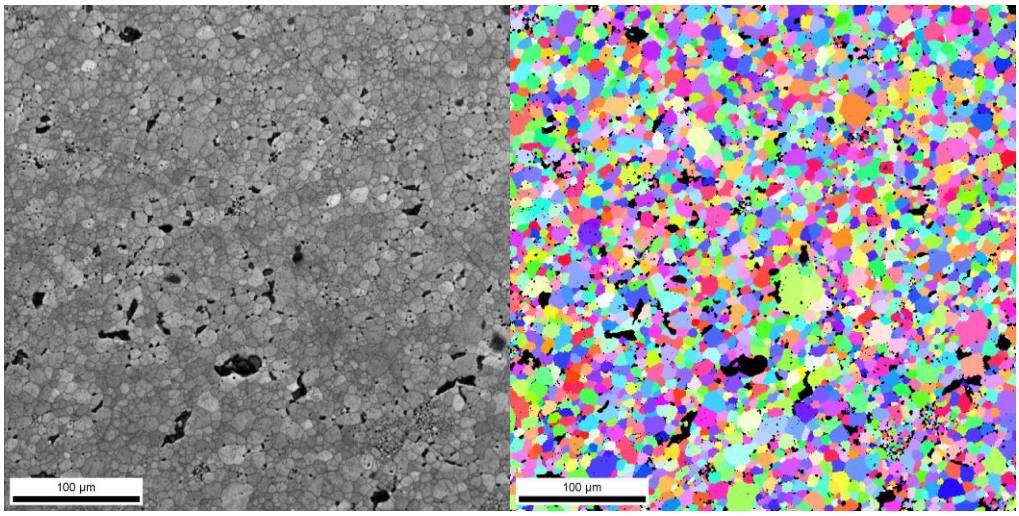

Figure 4.1: SEM and EBSD image of the UO_2 sample [31]

From the selected area, statistics of misorientation angle and CSL distributions for GBs were obtained from the EBSD map by EDAX-TSL OIM™ analysis software. The number fractions and distributions of CSL GBs are shown in Fig. 4.2. Note that the dominance of Σ3 GBs in the number fraction. It was observed that most Σ3 GBs were short in length and thus had a smaller length fraction; however, their distribution can still have a big impact on mass transport through the GBs as they can block the mass flow and force it to take other routes.

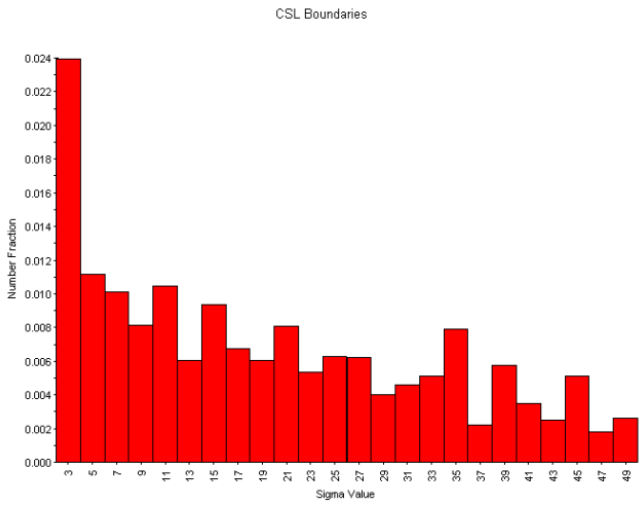

Figure 4.2: Distribution of CSL GBs in Number Fraction of the 200μm x 400μm [31]

The grain size and misorientation angle distributions are shown in Fig. 4.3. The sample had an average grain size of about 10μm and the highest misorientation angle fraction at about 42°. Most angles were located in the high diffusivity GB region. The total fraction of high angle GBs is 75% while 6.9% of them are CSL GBs, and thus the total high diffusivity GBs for this sample also had a fraction of 68%, a value higher than the critical percolation threshold calculated by Chen et al [13].

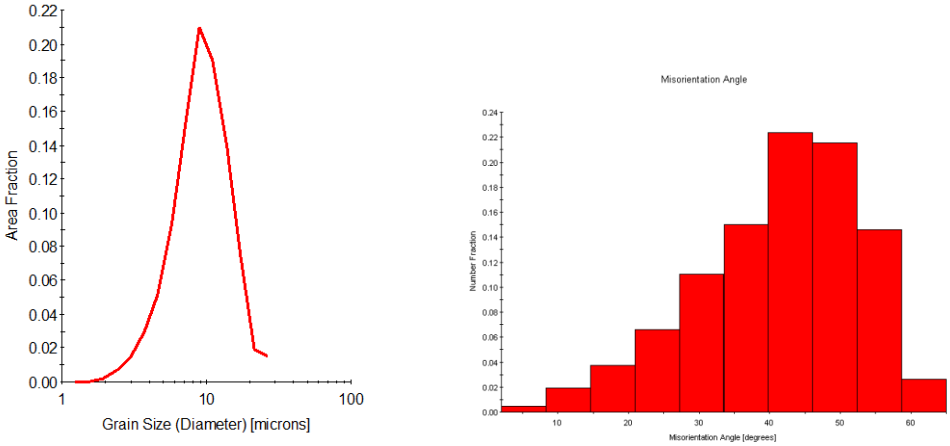

(a) (b)

Figure 4.3: (a) Grain size distribution (b) Misorientation angle distribution [31]

4.1.2 Grain Boundary Reconstruction and Distribution

The results of model reconstruction are shown in this section. Figure 4.4 shows the reconstructed 2-D GB network. The locations of low diffusivity GBs have a strong influence on the formation of percolation paths. The information of different GB distributions are collected by the OIM software and plotted in Fig. 4.5 where the GBs are assigned properties corresponding to high diffusivity, low diffusivity and bulk diffusivity GBs. The distributions shown here and the connectivity of the GB network will be used to analyze the simulation results. The CSL GBs here only include low Σ values up to Σ11 because the low Σ GBs have higher fractions in this sample and other characterized UO_2 samples [30]; moreover, experimental data of GB energy are better established for low Σ GBs and thus only Σ3 to Σ11 are considered in this study.

(a)

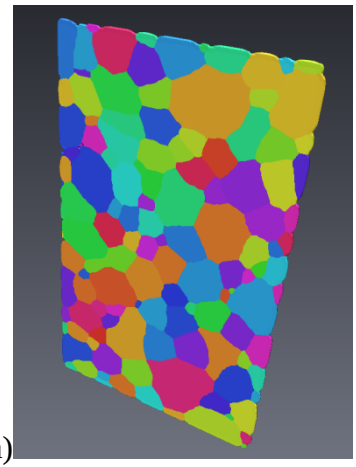

(b)

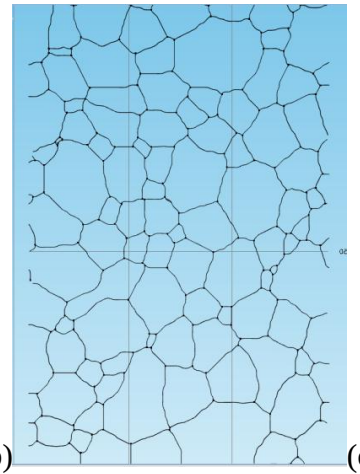

(c)

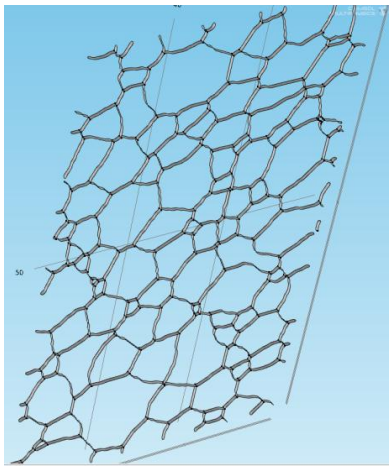

Figure 4.4: (a) Reconstructed 3-D microstructure model created in AVIZO™. (b), (c) A two dimensional grain boundary structure imported into COMSOL™.

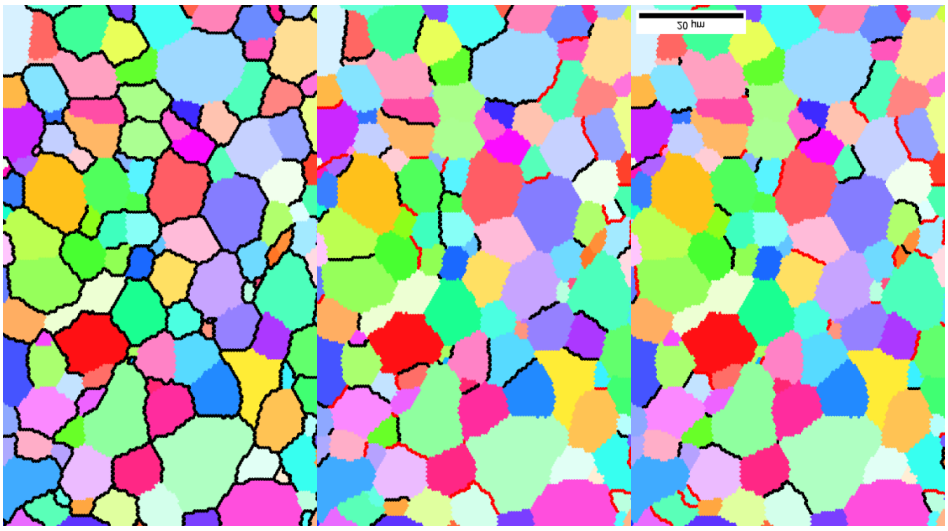

Figure 4.5: The distributions of (a) High Diffusivity GBs, (b) Low Diffusivity GBs and (c) Bulk Diffusivity GBs with CSL GBs labeled in red

4.2 Simulation: constant temperature with different diffusivity contrast

Previous simulations [6] on a UO_2 sample that demonstrated the presence of percolation paths at a diffusivity ratio higher than 10^4 were discussed in section 1.2.3. The sample studied here has the same fraction of high diffusivity GB of 68%. Based on the results shown in [13] and the results of this previous simulation [6], it is expected to see similar percolation behavior for the model created for this study. The simulation conducted in this section keeps the temperature constant. Without a heat transfer mechanism, diffusivity becomes the only temperature dependent material property. The value for temperature is taken as the average value across the temperature profile, which was obtained in Eq.3.3, and was calculated to be about 1600K. The boundary concentrations were set at the highest value (center of the pellet) and the lowest value (edge of the pellet) to stress the effects of mass transport. The model is set up to be a baseline to

compare with other cases that include various temperature and concentration gradients. Three diffusivity values are assigned to GBs according to Fig. 4.5, and the diffusivity contrasts of different GBs are varied from D_2/ D_{bulk}= 1, 10^2, 10^4, 10^6 and 10^8 with D_1 set as a geometric mean between the two.

The concentration profile was obtained for different contrasts as shown in Fig. 4.6. Note that region containing the grains should have a zero concentration, but the software interpolated their magnitude with respect to the GBs concentration around them and thus gives the profile in Fig. 4.6. The effect of different GB properties is obvious even at low D ratios as it can be seen that Fig. 4.6a has a uniform profile along the across the length of the model while the ones with different diffusivities (Fig. 4.6b, c and d) have a lower concentration gradient on the upper right corner compared to its left. It is the presence of many low diffusivity GBs on the upper left corner (see Fig. 4.5) that are blocking the mass flow and causing the shift in concentration. At high diffusivity contrast (Fig. 4.6d), the concentration also shifted to the lower left corner giving a flat surface at the lower right, again, reflecting the distribution of different GBs. The discontinuities exist wherever there is a transition from low to high diffusivity grain boundaries. The difference between Fig. 4.6b, c and d is not obvious as these are the results at the steady state.

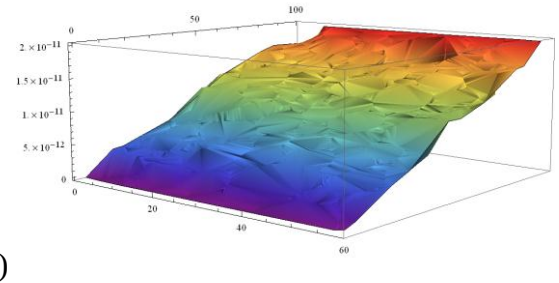

(a)

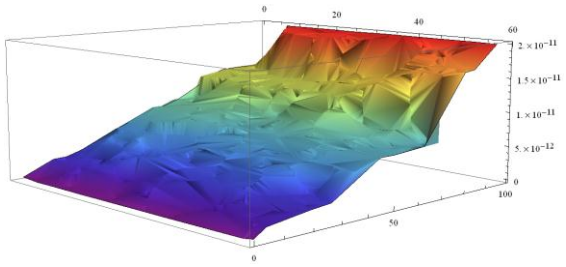

(b)

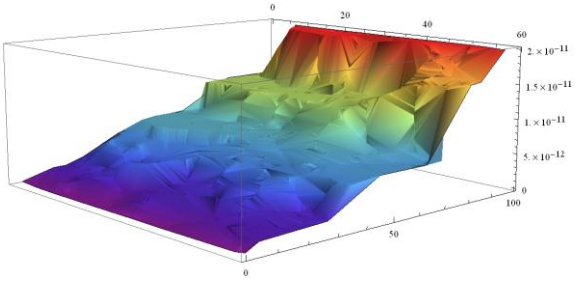

(c)

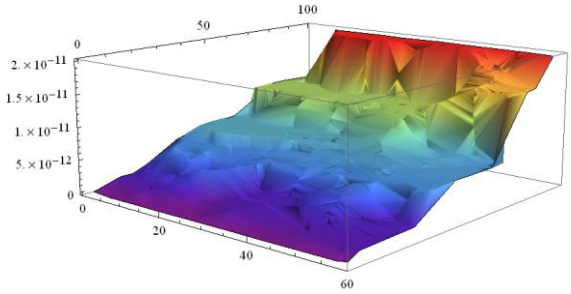

(d)

Figure 4.6: Concentration surface profile (mol/cm2) (a)$D_2/D_{bulk}=1$ (b)$D_2/D_{bulk}=10^2$ (c) $D_2/D_{bulk}=10^4$ (d) $D_2/D_{bulk}=10^8$

4.2.1 Mass Flux Profiles at Low Diffusivity Contrast

For the mass flux profiles, the results for the low diffusivity contrast cases are examined here. The profiles of mass flux are plotted in logarithmic scale due

to large variations in magnitudes as they are functions of diffusivity and concentration gradient as described by Fick's First Law. The macroscopic concentration gradient is the same for all runs in this study and thus the values of mass flux solely depends on the diffusivity of GB.

The mass flux for low diffusivity cases, from D_2/ D_{bulk}=1 to10^4, are plotted in In Fig. 4.7 where the changes in overall magnitude of mass flux can be seen clearly between profiles of different diffusivity ratios, but not much variance between GBs can be observed, except in Fig. 4.7d where certain regions have higher flux than others. The results here showed no significant effect of grain boundary diffusion at low diffusivity contrast, agreeing with the anlytical analysis and the previouse simulation model.

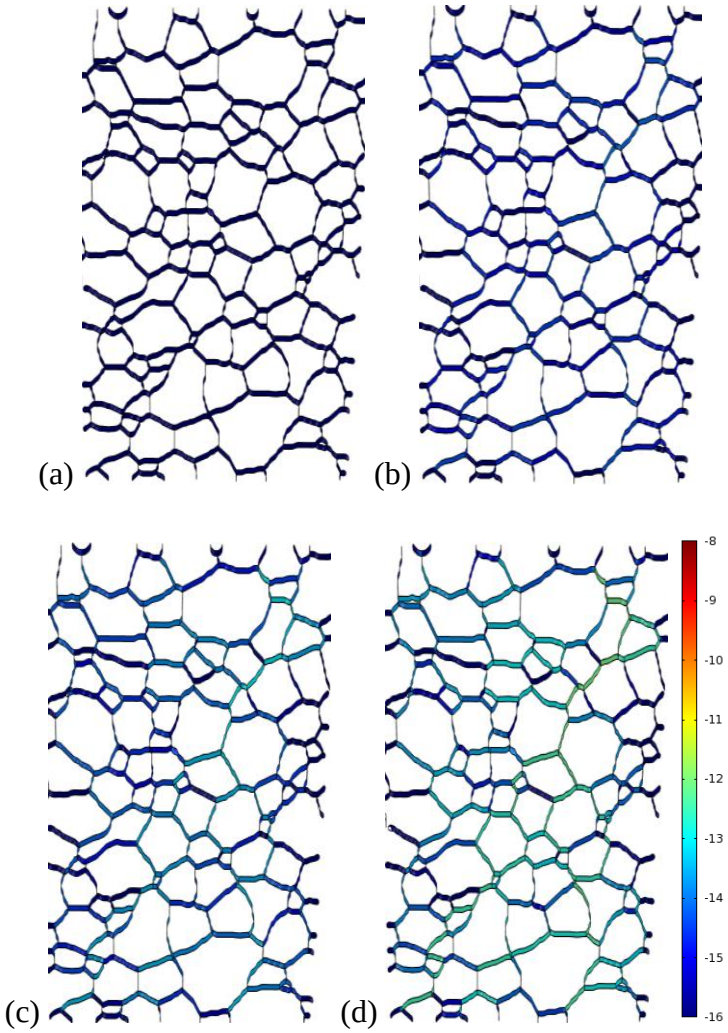

Figure 4.7: Magnitude of mass flux (mol/cm-s) in log scale: (a) $D_2/D_{bulk}=1$, $J_{max}=10^{-15.848}$ (b) $D_2/D_{bulk}=10^2$, $J_{max}=10^{-13.883}$ (c) $D_2/D_{bulk}=10^3$, $J_{max}=10^{-12.911}$ (d) $D_2/D_{bulk}=10^4$, $J_{max}=10^{-11.941}$

The difference between various diffusivity contrasts can be better observed in 3-D surface plots as shown in Fig. 4.8. The values of the grains are interpolated here just like the 3-D concentration surfaces. It can be seen that the flux magnitude in region that does not belong to the percolation paths starts to

fade out with the increase of the diffusivity contrasts; however their values are still observable in these low diffusivity contrast cases.

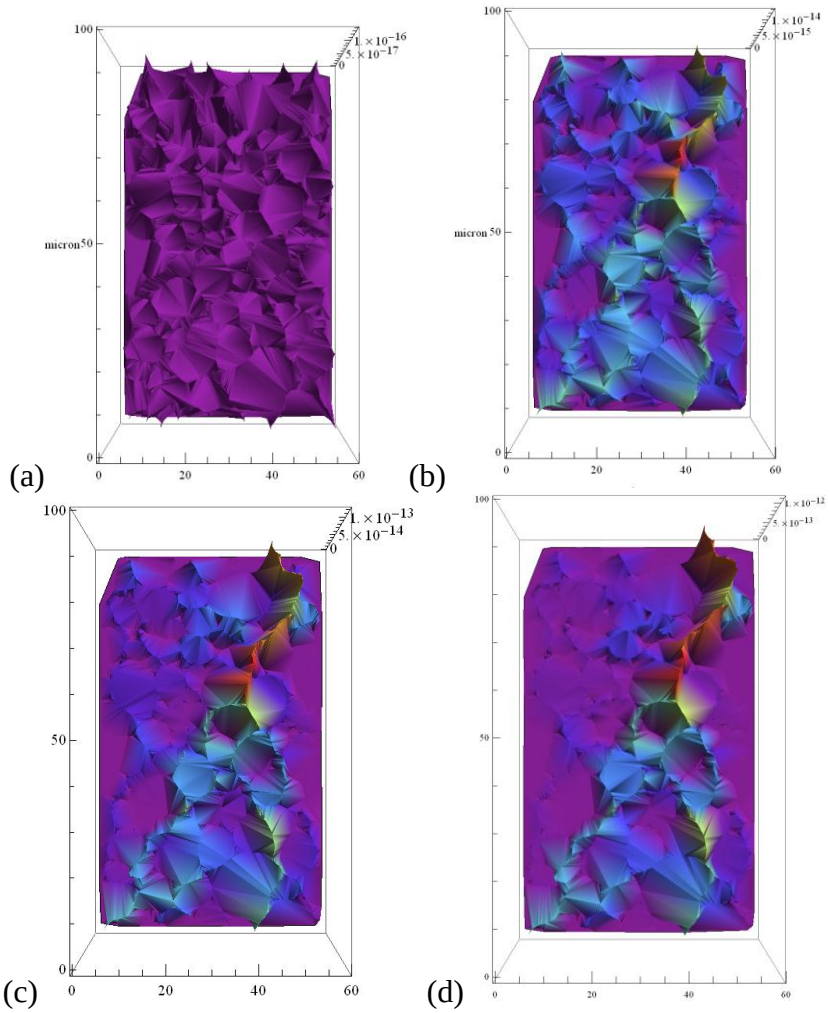

Figure 4.8: Mass Flux 3-D Surface Plots (mol/cm-s) (a) $D_2/D_{bulk}=1$ (b) $D_2/D_{bulk}=10^2$ (c) $D_2/D_{bulk}=10^3$ (d) $D_2/D_{bulk}=10^4$

4.2.2 Mass Flux Profiles at High Diffusivity Contrast

Mass profiles for high diffusivity contrast ($D_2/ D_{bulk}=10^5$ to 10^8) networks are shown in Fig. 4.9. As D_2/D_{bulk} ratio exceeds 10^4, simulations with high diffusivity contrast show localized mass flux occurring in GBs with higher diffusivity and percolation paths become more and more localized as the ratio

increases. The results agree with the past studies that showed the percolation behavior only at diffusivity ratios above 10^4. This value also agrees with Whipple's analytical solution to GB diffusion problem [51], which showed that an appreciable boundary penetration is observed only at a D_2/D_{bulk} ratio over $5x10^4$ for a GB thickness of $4x10^{-8}$cm and a bulk diffusivity of 10^{-11}.

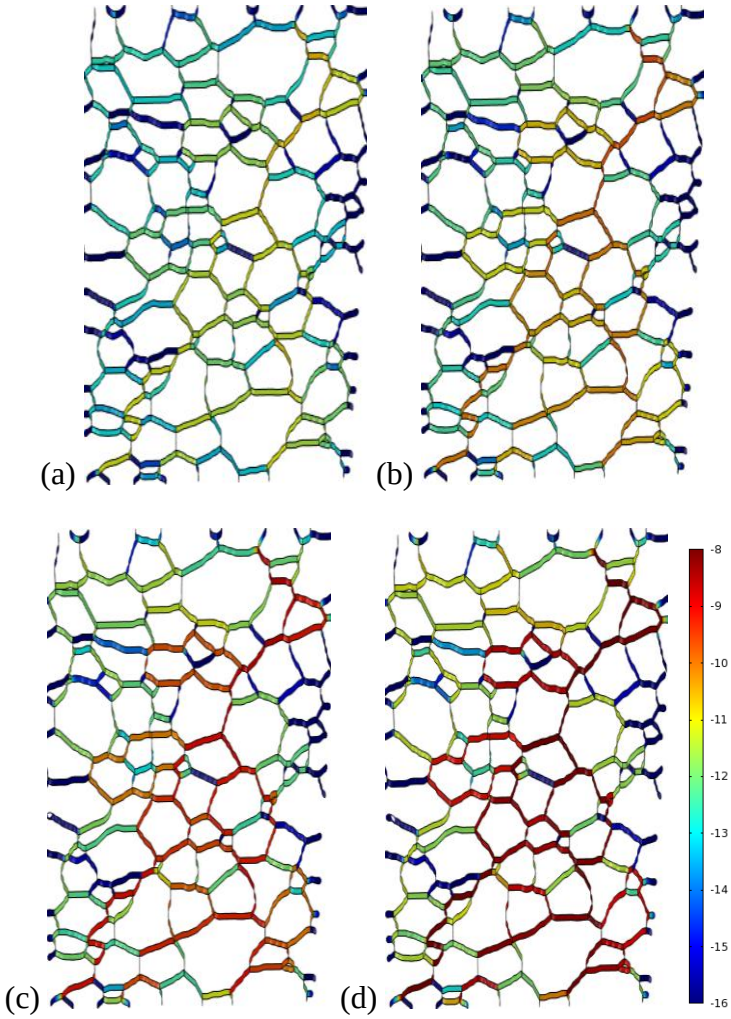

Figure 4.9: Magnitude of mass flux (mol/cm-s) in log scale: (a) $D_2/D_{bulk}=10^5$, $J_{max}= 10^{-10.931}$ (b) $D_2/D_{bulk}=10^6$,$J_{max}= 10^{-9.928}$ (c) $D_2/D_{bulk}=10^7$,$J_{max}=10^{-8.927}$ (d) $D_2/D_{bulk}=10^8$, $J_{max}=10^{-7.927}$

The 3-D mass flux surface profiles are again plotted for these high diffusivity contrast cases in order to observe the gradual change in the flux distribution and the formation of percolation paths. The flux magnitudes in the regions not on the percolation paths becomes not observable in the high diffusivity cases. Little or no difference in the 3-D surface can be observed between these high contrast cases which implies that the normalized effective diffusivity has reached a constant value as the diffusivity contrast exceeds its critical value of 10^4.

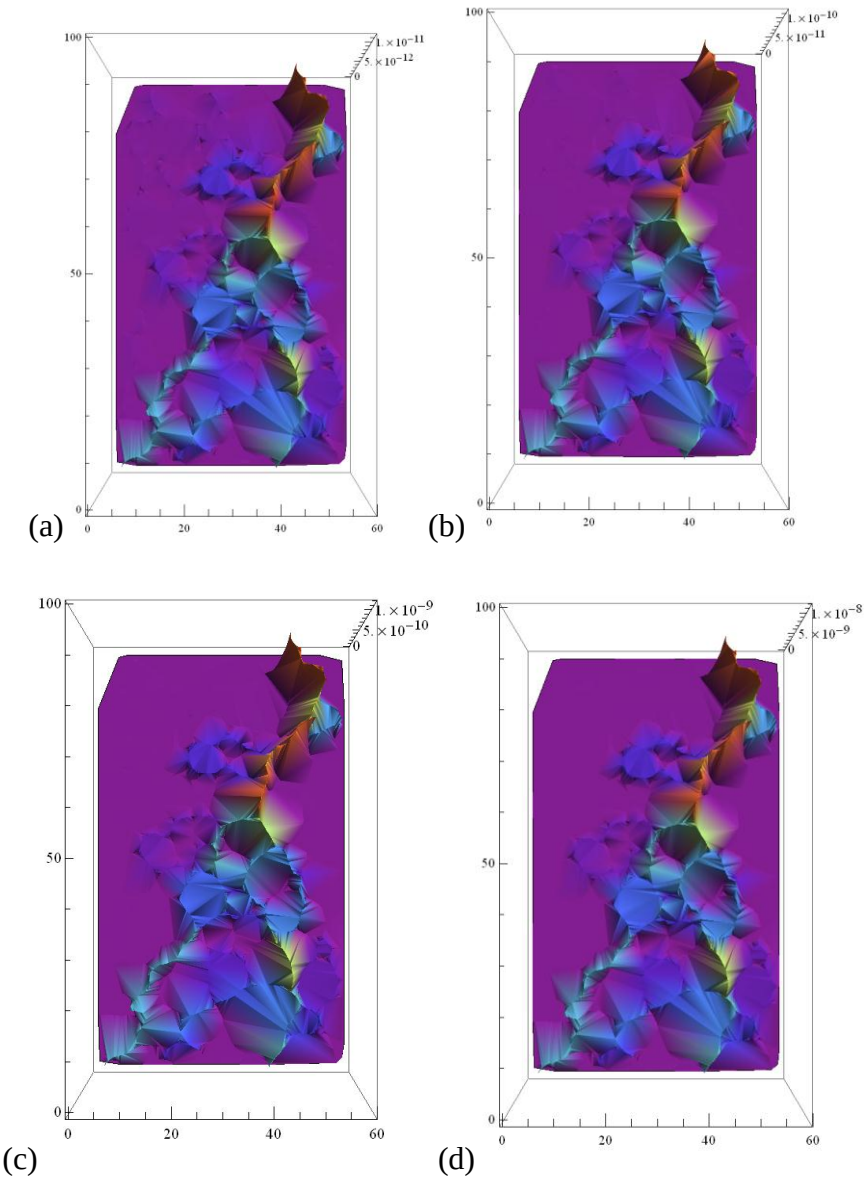

Figure 4.10: Mass Flux 3-D Surface Plots (mol/cm-s) (a) $D_2/D_{bulk}=10^5$ (b) $D_2/D_{bulk}=10^6$ (c) $D_2/D_{bulk}=10^7$ (d) $D_2/D_{bulk}=10^8$

The topology of the material containing only high diffusivity GBs is shown in Fig. 4.11a as a comparison with the mass flux profiles shown in Fig. 4.11b. It can be seen that there is a discontinuity at the top left corner, which explains the shift in concentration profiles as well as the way the percolation paths

form in the high diffusivity contrast profiles. In general, this set of simulations confirms effects of GBs on the formation of localized mass flow and validate of applying percolation theory on mass transport in this reconstructed 2-D GB network of UO_2.

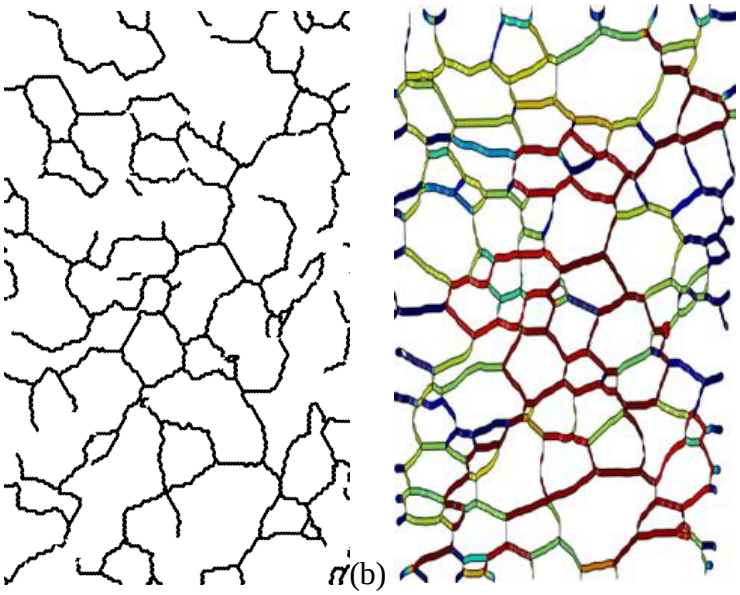

Figure 4.11: (a) High diffusivity GB network placing next to (b) $D_2/D_{bulk}=10^8$ mass flux profile to observe the percolation paths

4.3 Simulations: effects of temperature gradient on percolation paths

The capability of simulating multi-physics problems in COMSOL™ allows adding a temperature gradient to the model and thus simulating the behavior in a reactor better. Temperature has important effects on mass transport. In this regard, all material properties used in the model, including density, thermal conductivity, heat capacity and diffusivity, are temperature dependent and can

change significantly in the high temperature gradient within a pellet that is typical in a nuclear reactor.

This model keeps the same concentration gradient as section 4.2, and applies the full temperature gradient calculated across the radius of the pellet (2006K to 800K) to the model. The emphasis here is to see effect of temperature on concentration profiles as well as the mass flux and to compare with the constant temperature case illustrated in the previous section.

4.3.1 Effect of temperature on surface concentration and mass flux

The temperature gradient is applied as shown in Fig. 4.12a, and the corresponding concentration profiles along with mass flux magnitude profiles are shown in Fig. 4.12b and c at a diffusivity ratio of one. First of all, the temperature profile has a linear distribution vertically because all GBs are assigned with the same thermal properties of UO_2. A very sharp change in concentration is observed, which is caused by the changes in diffusivity with the temperature change. At high temperature regions, the diffusivity is high, but the concentration gradient does not have significant change until it reaches the boundary at the bottom. The high diffusivity GBs in the hot zone create a faster mass flow, which gives a more uniform concentration distribution in the steady state, until they reach the low diffusivity region where the flow is chocked by the low diffusivity GBs and thus forms a sharp drop in the profile. In fact, the concentration profile observed here reflects the one calculated numerically in the macroscale in Chapter III.

The mass flux profile with no diffusivity contrast looks similar to the temperature independent case since no localized mass flow is observed; however, it is noticed that it has a smaller maximum flux value. It is the low concentration gradient in the high temperature region that keeps the mass flux low. At the low temperature region, the decrease in diffusivity is more dominant than the concentration gradient, and thus the overall mass flux is smaller than the constant temperature simulation.

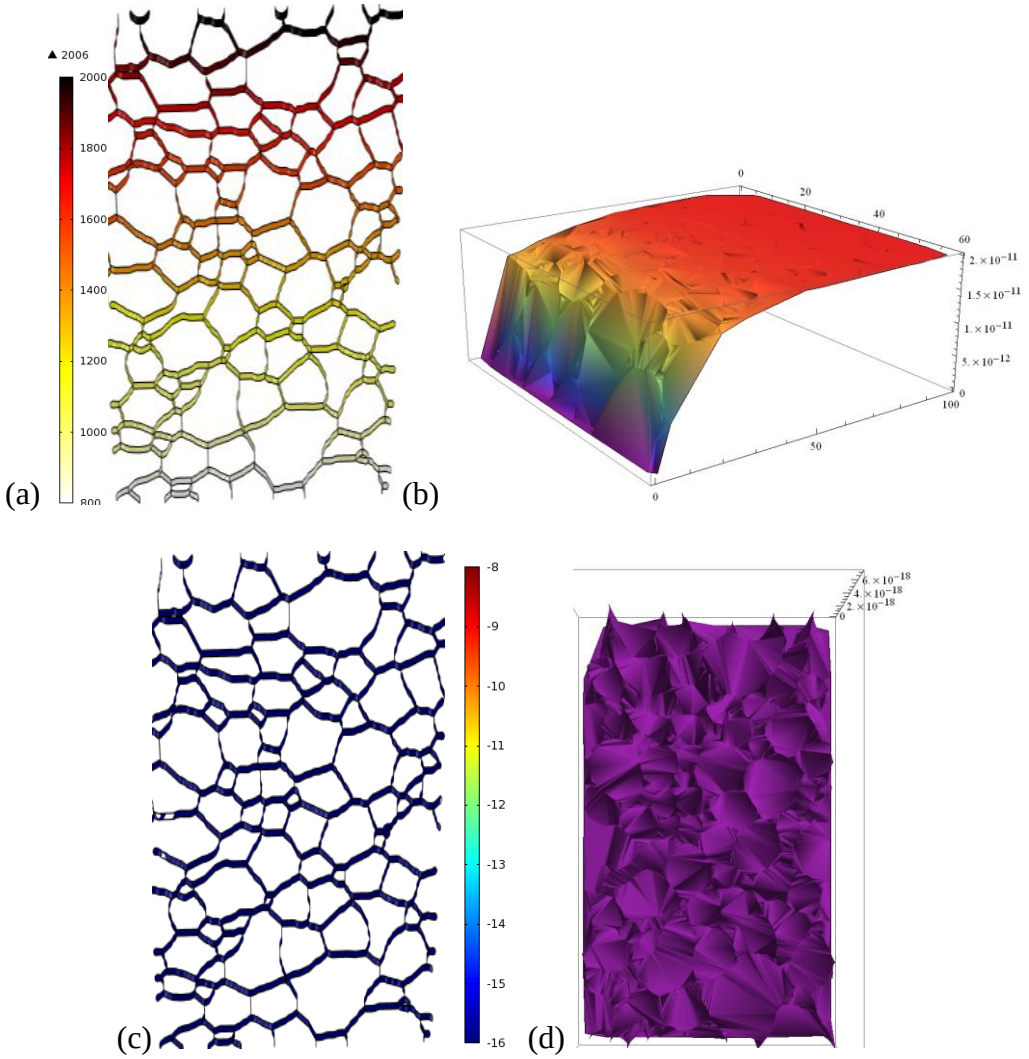

Figure 4.12: Effect of temperature on concentration and mass flux, D_2/D_{bulk} =1 (a) Temperature profile (b) Concentration profile (c) Magnitude of mass flux (mol/cm-s) in log scale, $J_{max}= 10^{-17.149}$ (d) 3-D Mass Flux Surface

4.3.2 Diffusivity contrast with Temperature Gradient

Now different diffusivity contrasts are applied to the model keeping the same overall temperature and concentration gradients. The temperature profile remains unchanged, as it is only affected by thermal conductivity, density and

heat capacity of UO_2 in this study. It is also assumed that all GBs have the same properties.

The concentration 3-D surface, mass flux profile and its 3-D surface are plotted for the contrast ratio of 10^4 in Fig. 4.13, as it is an important threshold for the observation of percolation behaviors. The distribution of high diffusivity GBs are also plotted in Fig. 4.13d, showing a connected path from the upper right corner to the bottom. Similar to the case with diffusivity ratio of one, no change in concentration is observed until the bottom half of the geometry. However, with the presence of diffusivity contrast, the concentration profile becomes unbalanced at the bottom half, with a higher concentration at the left. This can be explained by observing Fig. 4.13d, where most of the high diffusivity GBs are slanted toward the bottom left corner. The mass that follows the high diffusivity paths travels further and thus creates a higher concentration on the left hand side. The interface with a sharp drop in concentration is also shifted upward indicating the formation of high flux paths that are contributing to a more even concentration distribution.

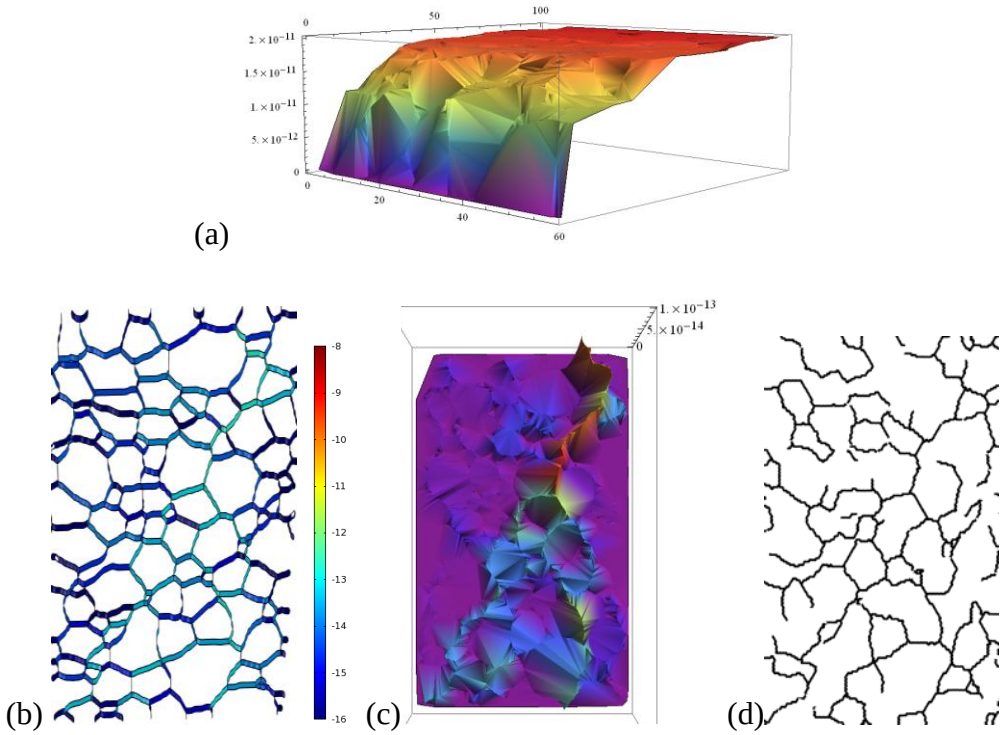

Figure 4.13: Effect of temperature on concentration and mass flux, $D_2/D_{bulk}=10^4$, (a) Concentration Profile (b) Magnitude of Mass Flux in log scale, $J_{max}=10^{-12.996}$(mol/cm*s) (c) 3-D Mass Flux Surface (d) Network of high diffusivity GBs

The highest contrast case is also plotted in Fig. 4.14 to see the behaviors under high diffusivity contrast. The behavior, in general, is similar to the diffusivity contrast of 10^4 but with a stronger effect: the concentration difference between the bottom left and the bottom right becomes larger, the sharp concentration drop interface is shifted higher, and the mass flux becomes more localized.

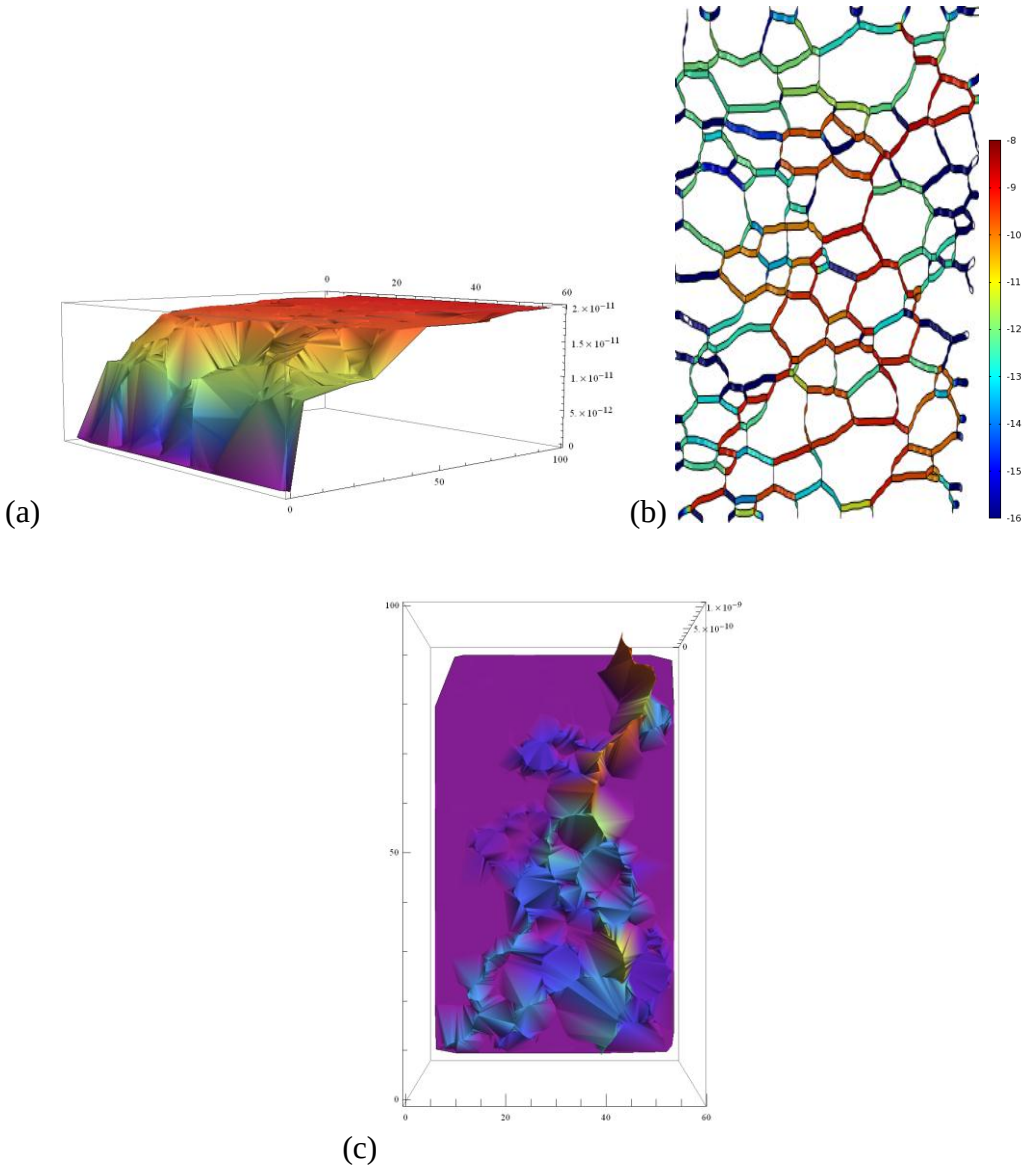

Figure 4.14: Effect of temperature on concentration and mass flux, $D_2/D_{bulk}=10^8$, (a) Concentration Profile (b) Magnitude of Mass Flux (mol/cm-s) in log scale, $J_{max}=10^{-8.962}$ (c) 3-D Mass Flux Surface

4.4 Simulation: Window method, different locations within a fuel pellet

The purposes of the simulations conducted in section 4.2 and 4.3 are to observe the formation of percolation paths and to see the effect of temperature

gradients. The applied boundary conditions were exaggerated for better observations. In this section, the window method is applied by placing the microstructural explicit model at different radial locations of a fuel pellet to observe the effect of diffusivity contrast on mass flux. The dimensions of the model as well as the applied boundary conditions reflect the real values of a fuel pellet inside a reactor. Note that in a reactor, the grain structures tend to be different at different locations due to irradiation effects that lead to pellet reconstruction; however, the microstructure is assumed to be uniform at the low burnup stage of the fuel cycle. The model here reflects the actual length scale of a pellet, and the boundary conditions are applied according to the concentration and temperature profiles obtained in Chapter III. These profiles are shown in Fig. 4.15 and Fig. 4.16. A table of different boundary condition values obtained from the profiles is given in Table 4.1 with the values used in the simulations highlighted. These highlighted values reflect the environments of the three regions illustrated in Fig. 4.17.

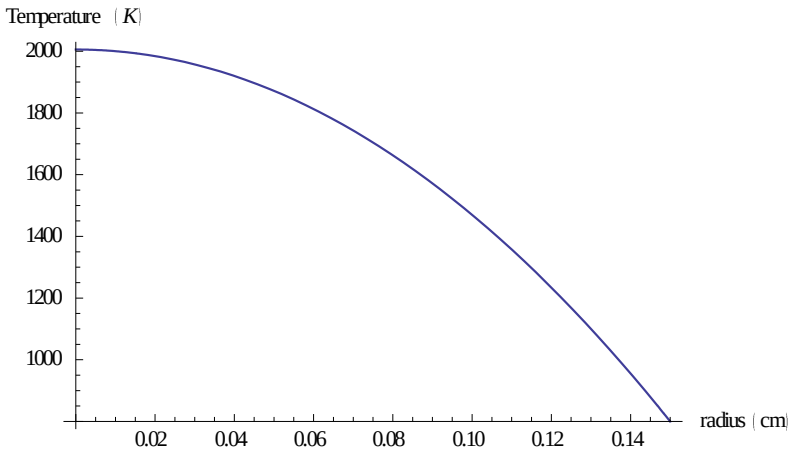

Figure 4.15: Concentration profile across the radius of the pellet

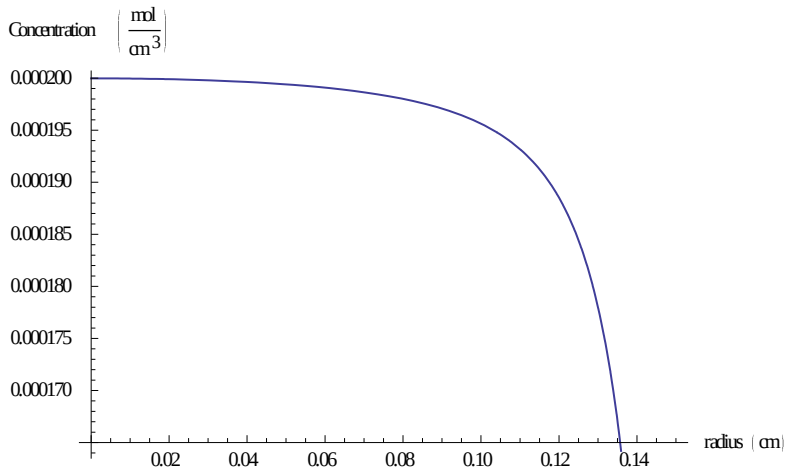

Figure 4.16: The plot of the calculated temperature profile along radius

Table 4.1: A list of boundary conditions across radius of the pellet. The highlighted values are applied in the model.

	Radial Position (cm)	Temperature (K)	Surface Concentration(10E-11mol/cm2)
Center	0	2006	1.99981
	0.01	2000	1.99961
	0.02	1984	1.99899
	0.03	1957	1.99792
	0.04	1920	1.99631
	0.05	1872	1.99403
Intermediate	0.06	1813	1.99085
	0.07	1743	1.98642
	0.08	1663	1.9801
	0.09	1572	1.97079
	0.1	1470	1.95628
edge	0.11	1357	1.93175
	0.12	1234	1.88521
	0.13	1100	1.78004
	0.14	955	1.46803
	0.15	800	0

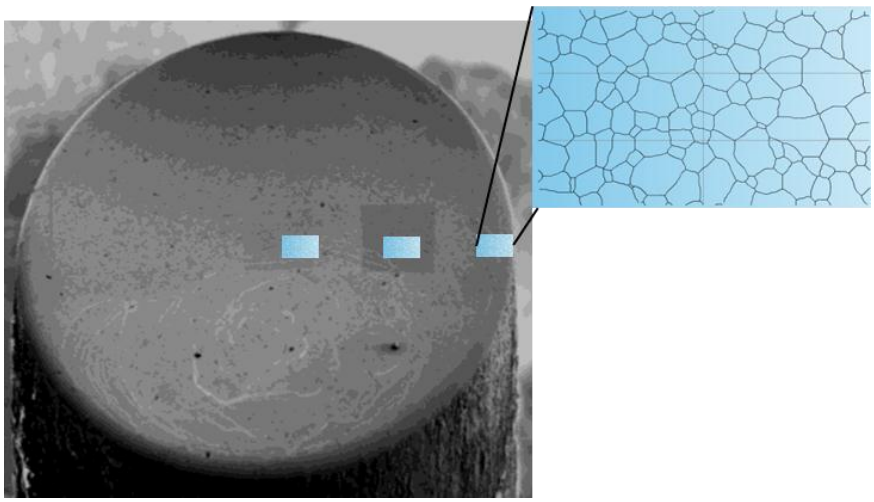

Figure 4.17: An illustration of window method

4.4.1 Center Region

Boundary Conditions: r_1=0cm, r_2=0.01cm, C_1= 1.99981x10^{-11} mol/cm^2, C_2=1.99961x10^{-11} mol/cm^2, T_1=2006K, T_2= 2000K

In this region, temperature is at the highest and thus gives the highest diffusivities, which create a low concentration profile as explained in the previous section. The temperature gradient here is also at the minimum according to the temperature profile obtained. Mass fluxes under these conditions are plotted in Fig. 4.18 with different diffusivity contrasts. Overall, the magnitude of mass flux has smaller values than the previous studies due to lower concentration gradients here. The percolation paths cannot be observed in the low diffusivity contrasts indicating the effect of GB diffusion on overall mass transport is small.

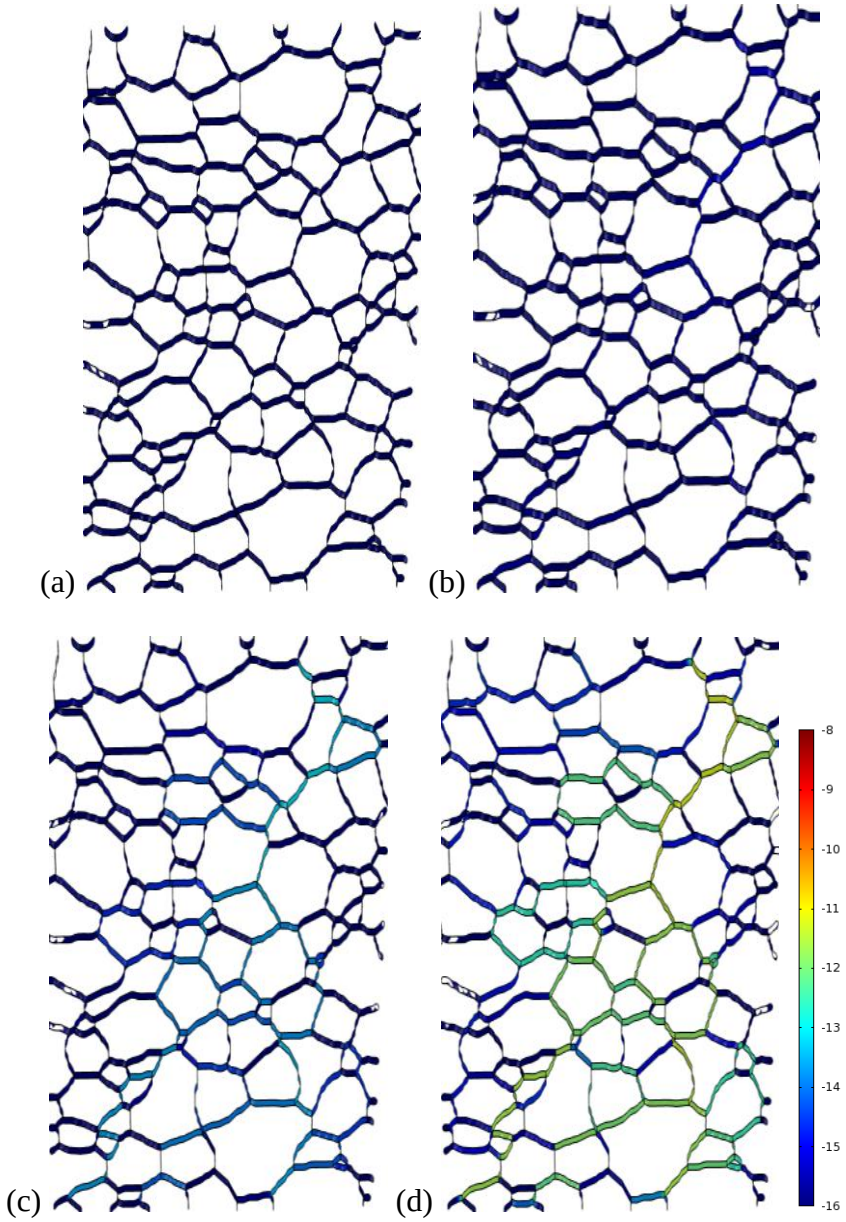

Figure 4.18: Center magnitude of mass flux (mol/cm-s) in log scale: (a) $D_2/D_{bulk}=1$: $J_{max}= 10^{-19.388}$ (b) $D_2/D_{bulk}=10^4$: $J_{max}= 10^{-15.48}$ (c) $D_2/D_{bulk}=10^6$: $J_{max}=10^{-13.467}$ (d) $D_2/D_{bulk}=10^8$: $Jmax=10^{-11.466}$

4.4.2 Intermediate Radial Position

Boundary Conditions: r_1=0.08cm, r_2=0.09cm, $C_1= 1.9801x10^{-11}$ mol/cm^2, $C_2= 1.97079x10^{-11}$ mol/cm^2, T_1=1663K, T_2=1572K

In the intermediate-radial region, the temperature and concentration gradients are higher than the center while the temperature is lower. The mass flux surface plots were obtained for the same four diffusivity contrasts as shown in Fig. 4.19. The magnitudes of the mass flux are higher, and thus a slight contrast in mass flux can be observed for diffusivity ratio of 10^4. As the diffusivity contrast increases, the flux turns more localized just like previous studies. The higher flux indicates that from center to the intermediate region, the concentration gradient has a stronger effect over the drop of diffusivity caused by temperature drop. To look closer to this change, the diffusivity profile along the radius is plotted in Fig. 4.20. The figure shows that the diffusivity drops only by half while the concentration gradient in the intermediate region is calculated to be 50 times higher.

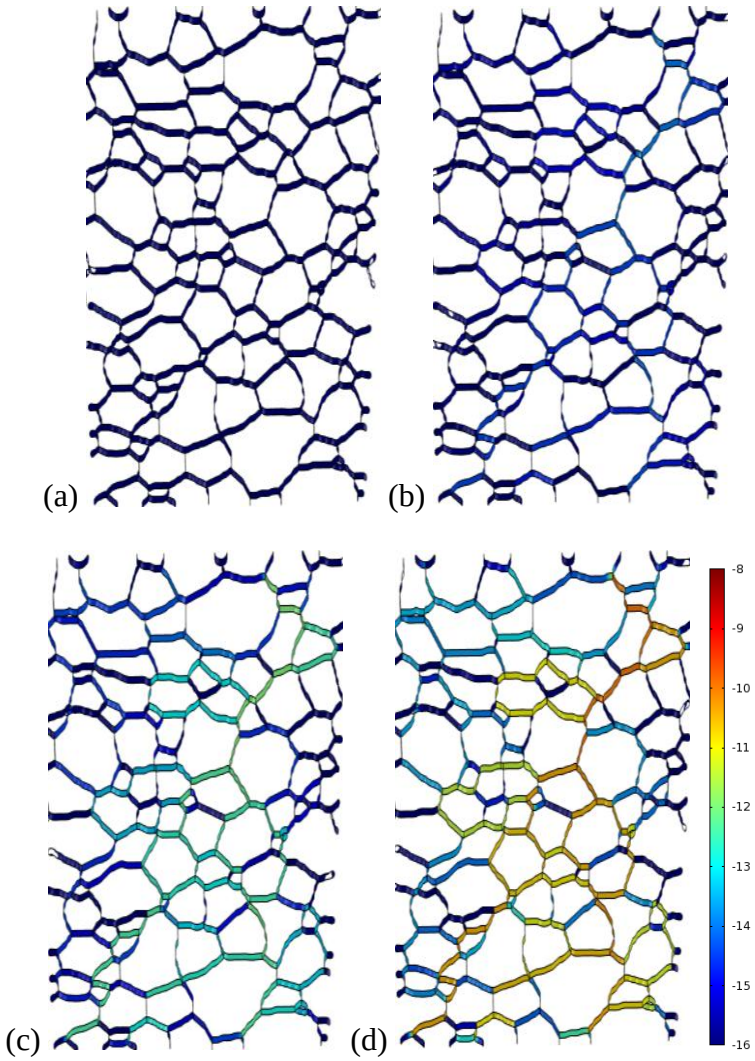

Figure 4.19: Intermediate region magnitude of mass flux (mol/cm-s) in log scale: (a) $D_2/D_{bulk}=1$: $J_{max}= 10^{-18.158}$ (b) $D_2/D_{bulk}=10^4$: $J_{max}= 10^{-14.237}$ (c) $D_2/D_{bulk}=10^6$: $J_{max}=10^{-12.224}$ (d) $D_2/D_{bulk}=10^8$: $J_{max}=10^{-10.223}$

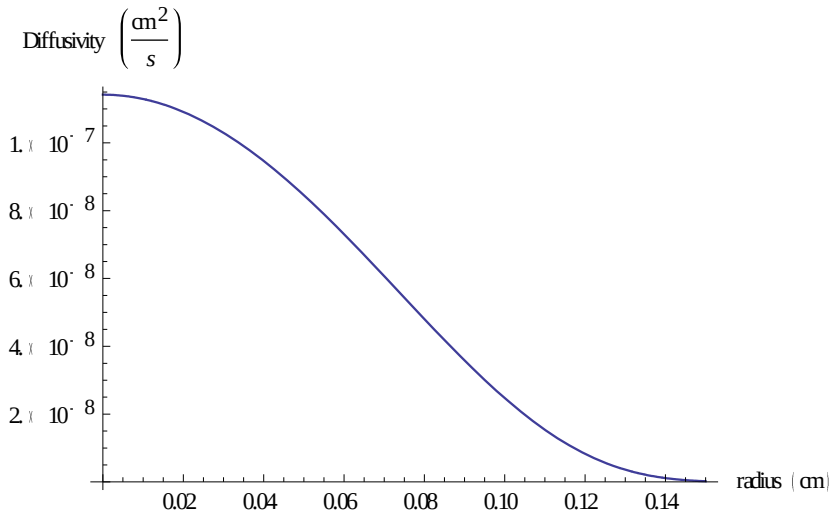

Figure 4.20: The value of bulk diffusivity across the radius of the pellet

4.4.3 Periphery Region

Boundary Conditions: r_1=0.14cm, r_2=0.15cm, C_1=1.46803x10^{-11}mol/cm^2, C_2=0 mol/cm^2, T_1=955K, T_2=800K

At the edge of the pellets, the temperature is the lowest but the temperature and the concentration gradients are the highest of the three windows. The same diffusivity contrasts were applied and the magnitudes of mass flux profiles are plotted in Fig.4.21. These runs give the highest values of mass flux under the high concentration gradient, and the percolation paths are the most obvious of the three locations which implies that the GB diffusion has the most significant effect at the edge of a fuel pellet. Having GB dominant diffusion at the edge of a pellet implies that GB plays an important role in fission gas release, a simulation result that agrees with the analytical work by Olander [20].

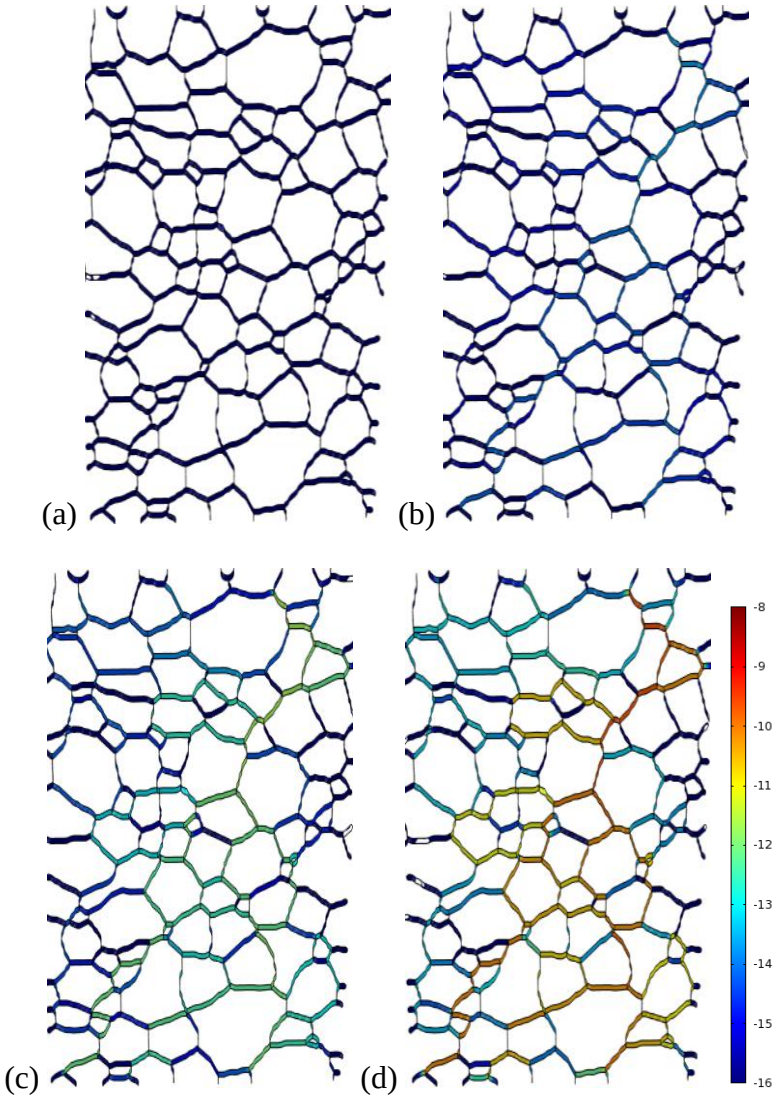

Figure 4.21: Edge magnitude of mass flux (mol/cm-s) in log scale: (a) $D_2/D_{bulk}=1$: $J_{max}= 10^{-17.936}$ (b) $D_2/D_{bulk}=10^4$: $J_{max}= 10^{-13.947}$ (c) $D_2/D_{bulk}=10^6$: $J_{max}=10^{-11.932}$ (d) $D_2/D_{bulk}=10^8$: $J_{max}=10^{-9.931}$

To summarize the three cases simulated in section 4.4, the values of maximum mass flux are ranked in the following order: Periphery> Intermediate > Center. In the literature [19], Olander indicated that the fission gas diffusivity is the highest at the center while the lowest at the edge due to the effect of temperature. The results presented here showed the phenomena after steady state

is reached. The high diffusivity resulted in a high and uniform concentration profile until it reached the edge where the concentration drops because of lower mobility and a larger circumference cross section. The magnitude of mass flux, at steady state, is affected by the concentration at its equilibrium, and has the lowest value at the center while the highest at the edge in order to have a continuous mass flow across the radius.

The percolation paths become more significant moving from the center to the edge of a fuel pellet, indicating that GB diffusion dominates at the edge while having minimal effects in the high temperature region. This role GBs play at the edge of a fuel pellet, however, can be engineered to control the release of fission products. For example, if low diffusivity GBs can surround the edge of a pellet, they can block the movement of fission products and retain them inside the pellet for a longer period of time. Even after the pellet restructures, the edge region still possesses the same microstructure, which would allow the GB effects to work at higher burnup as well.

Another finding in this chapter is the effects of percolation paths on concentration profiles. High diffusivity paths can create a more uniform concentration profile as discussed in section 4.3. This property can also be utilized to ease the uneven distribution of fission products, which can cause stress concentration in some regions, of the pellet.

V CONCLUSIONS AND FUTURE WORK

5.1 Conclusions

This study began with an overview of nuclear power and the behaviors of oxide fuel pellets inside an LWR reactor. Past studies on the microstructural effects on fission gas diffusion were introduced, and the purpose of this study was introduced as the formulation of a modeling framework to investigate the effects of GB diffusivity and to observe percolation behaviors at different diffusivity contrasts for experimentally measured microstructures in UO_2. The work was based on the microstructural characterization of a UO_2 sample, the reconstruction of a finite element model based on the measured microstructure and the simulation of mass transport along the GB network based on different scenarios.

The following conclusions are drawn from the results of simulations:

1. A 2-D GB network model for finite element analysis was created based on a real microstructure of UO_2 with the experimentally obtained material properties incorporated. The model demonstrated the capability to overcome the issues present in previous modeling attempts, such as thick GBs, boundary conditions that are not directly related to physical conditions and the lack of multi-physics capabilities.
2. The constant temperature simulation demonstrated that the mass transport model can be applied on a real 2-D GB network of UO_2. The percolation paths were observed at a diffusivity ratio above 10^4, illustrating the effects of GBs can have on the distribution of fission gases. The paths of high diffusivity GBs also affect the distribution of fission gas concentration.

3. The presence of a temperature gradient created a uniform concentration profile in the high temperature region with a sharp drop before the low temperature boundary. At high diffusivity contrast, the concentration turned slightly more uniform due to the formation of high diffusivity paths which distributed the fission gases further. This implies the probability of preventing the regions with high concentration of fission products, which can be a source of failure.
4. Window methods were applied to see how fission products behave at different radial positions of a pellet. The difference in diffusivity, due to temperature, resulted in a uniform concentration profile at the center while drops sharply when it gets close to the edge. The relationship between the concentration gradient and the diffusivity creates a continuous flux across radius. The results of simulations showed that the GB diffusion has small effects on the transport of fission gases at the center of a pellet, while the effects become significant at the edge, the location that is the most relevant to fission gas release at low burnup. The edge of a restructured pellet is also the relatively unaffected area and can be engineered to control the fission gas release mechanism even at medium or high burnup.

5.2 Future work:

A significant number of additional features can be built on the current model. First of all, the same simulation can be conducted on the 3-D geometry, of which the GBs curvature through the thickness will be taken into account, and

study the mass flux through the thickness. More serial sectioning needs to be done to build on the thickness of the geometry. An ideal model should have a thickness that contains at least one complete grain in it for better observation of GB diffusion effects in a 3-D network.

With a 3-D geometry, triple junctions, the line where GBs meet, can be incorporated in the analysis. The differences in triple junction dihedral angles are results of the variation in interface energy which is closely related to GB energies [21]. With a 3-D reconstruction model, real triple junction dihedral angles can be measured, and analysis can be conducted to find the GB energies of the UO_2 sample and to observe how they are compared with the misorientation angles and CSL GBs.

In the current model, the heat and mass generation terms are only incorporated in the calculation of boundary conditions, but not in the model setup. In a nuclear reactor, fission products and heat are constantly generated from the bulk of the grains, and thus a model better representing the fuel elements should have grain elements that generate heat and fission products. Segregation of fission gases from grains to GBs can only be observed in such a model.

More complicated physics that are common in UO_2 fuels can be incorporated into the model. For examples, the fission gas diffusivity is also affected by the temperature gradient and irradiation, which should to be considered to make it a complete diffusion simulation. Mass transport along GBs also leads to some failure mechanisms such as coble creep which can be simulated with the model.

REFERENCES

1. Carbajo, JJ. "A Review of the Thermophysical Properties of MOX and UO2 Fuels." *Journal of Nuclear Materials* 299.3 (2001): 181-98.

2. Mihaila, Bogdan, et al. "Simulations of Coupled Heat Transport, Oxygen Diffusion, and Thermal Expansion in UO2 Nuclear Fuel Elements." *Journal of Nuclear Materials* 394.2-3 (2009): 182-9

3. FRISKNEY, C. "The Characteristics of Fission Gas Release from Monocrystalline Uranium Dioxide during Irradiation." *Journal of Nuclear Materials* 68.2 (1977): 186-92. Print.

4. Newman, Chris, Glen Hansen, and Derek Gaston. "Three Dimensional Coupled Simulation of Thermomechanics, Heat, and Oxygen Diffusion in Nuclear Fuel Rods." *Journal of Nuclear Materials* 392.1 (2009): 6-15.

5. HIRAI, M. "DIFFUSIVITIES OF FISSION-GAS SPECIES IN UO2 AND (U,GD)O-2 NUCLEAR-FUELS DURING IRRADIATION." *Journal of Nuclear Materials* 226.1-2 (1995): 238-51.

6. Rudman, K.; Krishnan, K.
Structure-Property Relations in Depleted Uranium Oxide: 3-D Microstructure Reconstruction and Mass Transfer Simulations., 2011.

7. Wheeler, K. "
Determination of Basic Structure-Property Relations for Processing and Modeling of
Advanced Nuclear Fuels: Microstructural Evolution and Multi-Scale Characterization." PhD Thesis Arizona State University, 2010. Web.

8. Kumar, P. P., and S. Yashonath. "Ionic Conduction in the Solid State." *Journal of Chemical Sciences* 118.1 (2006): 135-54.

9. Lemehov, S. "In-Pile Xe Diffusion Coefficient in UO2 Determined from the Modeling of Intragranular Bubble Growth and Destruction Under Irradiation." *Journal of Nuclear Materials* 374.3 (2007): 461-72.

10. Li, Mo. "Topological and Atomic Scale Characterization of Grain Boundary Networks in Polycrystalline and Nanocrystalline Materials." *Progress in materials science* 56.6 (2011): 864.

11. Olander, D. "Nuclear Fuels - Present and Future." *Journal of Nuclear Materials* 389.1 (2009): 1-22.

12. Pankaj V. Nerikar, Karin Rudman. "
Grain Boundaries in Uranium Dioxide: Scanning Electron Microscopy Experiments and Atomistic Simulations." *The American Ceramic Society* (2011).

13. Chen, Y. and C.A. Schuh, *Diffusion on grain boundary networks: Percolation theory and effective medium approximations.* Acta mater., 2006. 54: p. 4709-4720.

14. "Percolation of Diffusional Creep: A New Universality Class." *Physical Review Letters* 98.3 (2007).

15. Fisher, S. B., et al. "Microstructure of Irradiated SBR MOX Fuel and its Relationship to Fission Gas Release." *Journal of Nuclear Materials* 306.2-3 (2002): 153-72.

16. Y.S. Kim, G.L.H., *AAA Fuels Handbook*: Argonne National Laboratory, Argonne, Illinois: U.S. Department of Energy under Contract W-31-109-Eng-38.

17. Mihaila, Bogdan. "Simulations of Coupled Heat Transport, Oxygen Diffusion, and Thermal Expansion in UO2 Nuclear Fuel Elements." *Journal of Nuclear Materials* 394.2-3 (2009): 182-9

18. Hansen, Glen. "Three Dimensional Coupled Simulation of Thermomechanics, Heat, and Oxygen Diffusion in UO2 Nuclear Fuel Rods." *Journal of Nuclear Materials* 392.1 (2009): 6-15

19. Olander, D. *Fundamental Aspects of Nuclear Reactor Fuel Element*. United States of America: Technical Information Center, Office of Public Affairs Energy Research and Development Administration, 1976.

20. Olander, D. R., and P. Van Uffelen. "On the Role of Grain Boundary Diffusion in Fission Gas Release." *Journal of Nuclear Materials* 288.2-3 (2001): 137-47.

21. Rohrer, Gregory. "Grain Boundary Energy Anisotropy: A Review." *Journal of Materials Science* 46.18 (2011): 5881-95.

22. Duderstadt, J. and Hamilton, L. *Nuclear Reactor Analysis*. 1980, The University of Michigan, Ann Arbor, Michigan: John Wiley & Sons.

23. Ma Q, B.R., *Diffusion along [001] tilt boundaries in the Au/Ag system-I Experimental results.* Acta metal. mater., 1993. 41.

24. Cristea, Petrica. "Simulations of Coupled Heat Transport, Oxygen Diffusion, and Thermal Expansion in UO2 Nuclear Fuel Elements." *Journal of Nuclear Materials* 394.2-3 (2009): 182-9

25. Hansen, Glen. "Three Dimensional Coupled Simulation of Thermomechanics, Heat, and Oxygen Diffusion in UO2 Nuclear Fuel Rods." *Journal of Nuclear Materials* 392.1 (2009): 6-15

26. Turnbull, J. A., et al. "The Diffusion Coefficients of Gaseous and Volatile Species during the Irradiation of Uranium Dioxide." *Journal of Nuclear Materials* 107.2-3 (1982): 168-84.

27. D. Davies and G. Long, c (1963).

28. M.E. Meek and B.F. Rider, Compilation of fission product yields, NEDO-12154 (1972)

29. EDAX. *www.edax.com*. 2009 [cited; Available from: www.edax.com.

30. K. Rudman, K. Krishnan, and P. Peralta. *Structure-Property Relations in Depleted Uranium Oxide: Grain Boundary Statistics and Simulations using Mass Transfer Model*. 2 Vol. , 2010.

31. K. Rudman, R. McDonald, H. Lim, P. Peralta, E. Luther and K. McClellan. "Spatial and Crystallographic Correlations of Microstructural Features in Depleted Uranium Oxide." *Journal of Nuclear Materials(to be submitted)* (2011)

32. "Nuclear Power Today." Feb 2011 2011.Web. World Nuclear Association. <http://www.world-nuclear.org/info/inf01.html>

33. Graham Jr., ThomasHecker, Siegfried S.Reis, Victor H.Moniz, Ernest J.Pellaud, Bruno. "Preventing Nuclear Proliferation." *Issues In Science & Technology* 20.4 (2004): 5. *MAS Ultra - School Edition*. Web. 3 Nov. 2011

34. Salvatores, M., et al. "Nuclear Waste Transmutation." *Applied Radiation and Isotopes* 46.6-7 (1995): 681-7.

35. Was, Gary S., MyiLibrary, and SpringerLink. *Fundamentals of Radiation Materials Science*. Berlin; New York: Springer, 2007

36. Advanced Nuclear Power Reactors". *Information Papers*. World Nuclear Association. July 2008. http://www.world-nuclear.org/info/inf08.html. Retrieved 2 Nov. 2011

37. Edsinger, Kurt. "LWR Pellet-Cladding Interactions: Materials Solutions to SCC." *JOM (1989)* 53.7 (2001): 9-13.

38. Park, Sang Yoon, et al. "Effects of the Microstructure and Alloying Elements on the Iodine-Induced Stress-Corrosion Cracking Behavior of Nuclear Fuel Claddings." *Journal of Nuclear Materials* 376.1 (2008): 98-107.

39. Preis, W., and W. Sitte. "Modeling of Fast Diffusion Along Grain Boundaries in Oxide Ceramics." *Solid State Ionics* 179.21-26 (2008): 765-70.

40. Stubican, V. S., and J. W. Osenbach. "Influence of Anisotropy and Doping on Grain Boundary Diffusion in Oxide Systems." *Solid State Ionics* 12.0 (1984): 375-81

41. Rudman, K., et al. *Structure-Property Relations in Depleted Uranium Oxide: Grain Boundary Statistics and Simulations using Mass Transfer Model*. Los Alamos National Lab Research Report:, 2011.

42. OECD, and Nuclear Energy Agency. *Fission Gas Behaviour in Water Reactor Fuels*. Organisation for Economic Co-operation and Development, 2002.

43. Gao, Y. X., et al. "A Micro-Cell Model of the Effect of Microstructure and Defects on Fatigue Resistance in Cast Aluminum Alloys." *Acta Materialia* 52.19 (2004): 5435-49.

44. Mishin, Y., and Chr Herzig. "Grain Boundary Diffusion: Recent Progress and Future Research." *Materials Science and Engineering: A* 260.1-2 (1999): 55-71.

45. Swaroop, Sathya, et al. "Lattice and Grain Boundary Diffusion of Cations in 3YTZ Analyzed using SIMS." *Acta Materialia* 53.19 (2005): 4975-85

46. Mistler, R. E., and R. L. Coble. "Grain-Boundary Diffusion and Boundary Widths in Metals and Ceramics." *Journal of Applied Physics* 45.4 (1974): 1507-9.

47. Fielitz, P., et al. "Aluminium Grain Boundary Diffusion in Polycrystalline Mullite Ceramics." *Physics and Chemistry of Minerals* 34.6 (2007): 431-6.

48. Sutton, A. P., and R. W. Balluffi. *Interfaces in Crystalline Materials*. 51 Vol. Oxford England: Clarendon Press, 1995

49. Porter, David A, and K. E Easterling. Phase Transformations In Metals And Alloys. 2nd ed. London: Chapman & Hall, 1992

50. Fisher, J. C. "Calculations of Diffusion Penetration Curves for Surface and Grain Boundary Diffusion." *Journal of Applied Physics* 22.1 (1951): 74-7

51. Shewmon, Paul G. *Diffusion in Solids*. New York: McGraw, 1963

52. Whipple, R. T. P. "Concentration Contours in Grain Boundary Diffusion." *Philosophical magazine (Abingdon, England)* 45.371 (1954): 1225-36.

53. Inderjeet Kaur, Yuri Mishin, and Wolfgang Gust. *Fundamentals of Grain and Interphase Boundary Diffusion*. 3 rev a enl ed. Chichester; New York: John Wiley, 1995.

54. Fisher, Craig A. J., and Hideaki Matsubara. "The Influence of Grain Boundary Misorientation on Ionic Conductivity in YSZ." *Journal of the European Ceramic Society* 19.6-7 (1999): 703-7.

55. Kingery, W. D., H. Kent Bowen, and Donald Robert Ulhmann. *Introduction to Ceramics*. 2nd ed. New York: Wiley, 1976

56. Stauffer, Dietrich. *Introduction to Percolation Theory*. London; Philadelphia: Taylor & Francis, 1985